JULIUS-MAXIMILANS-UNIVERSITÄT WÜRZBURG

Faculty of Physics and Astronomy

Chair for Astronomy

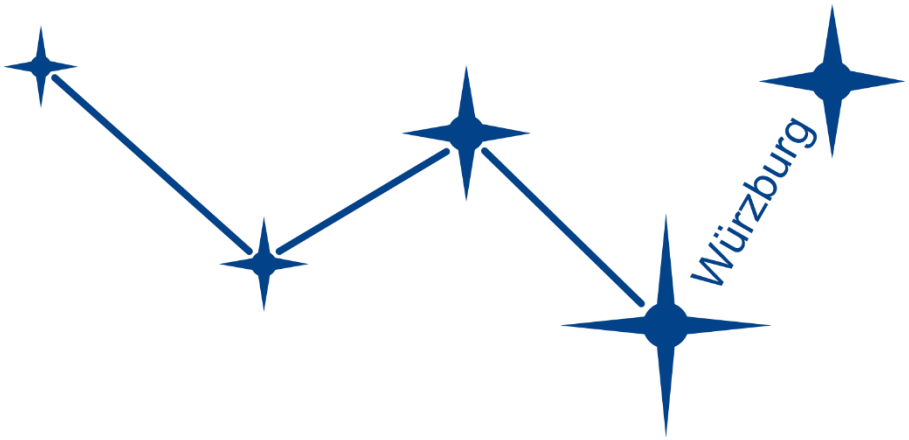

Bachelor Thesis

VLBI Properties of Candidate Neutrino-Emitting Blazars

Author:	Philip Weber
Supervisor:	Prof. Dr. Matthias Kadler
Date of submission:	February 10, 2020

Abstract

Active galactic nuclei are some of the most powerful and luminous objects known in modern astrophysics. In the optical band, the cores of these usually elliptical galaxies can reach luminosities of similar magnitude as the rest of the galaxy. They are bright among almost all wavelengths, and can produce bipolar streams of hot plasma, called jets, that can surpass its host galaxy in size. These jets are observed in the radio band with the technique Very Long Baseline Interferometry. This method uses multiple radio telescopes to create high-resolution images of astrophysical sources. It allows us to analyse active galactic nuclei, of which many have a redshift larger than 0.1, on a scale of only a few parsecs. In the special case of the jet pointing directly towards the observer, these sources are classified as blazars. So far, blazars are the most luminous known objects in astrophysics, that have a relatively constant flux.

Neutrinos are elementary particles that are part of the Standard model. They are very hard to detect and can be produced in almost any elementary scattering process, that involves the weak nuclear force. Since 2010 the IceCube Telescope has been observing astrophysical neutrinos. The sun, the supernovae 1987A and muon scattering in earth's atmosphere are known to produce neutrinos. However, to date it is not exactly clear where high-energy neutrinos originate from.

It was already theorised in the 1990s, that active galactic nuclei, especially their subclass, the blazars, could be responsible for the production of neutrinos with energies over 10 TeV. The detection of the neutrino IC-170922A was one of the first measurements supporting this theory with a high certainty. It was found in spatial coincdence to the blazar TXS 0506+056. The IceCube collaboration claims that there is a 3σ confidence, that this source and the neutrino can be associated. This led to the search for other active galactic nuclei that are in spatial coincidence with high-energy neutrino events.

This thesis focuses on four candidate neutrino sources, TXS 0506+056, PKS 0723-008, 4C +06.41 and PKS 1502+106. The radio properties of these sources are analysed to find out, whether they show any kind of unusual behaviour that could possibly be related to the production of high energy neutrinos. The four sources are examined regarding flux density, kinematics, morphology and polarisation. However, none of them really stand out when compared to the MOJAVE blazar sample that is used to portray the average blazars. Only 1502+106 seems to be a relatively bright flat spectrum radio quasar that shows quite high jet speeds.

To establish, whether the four analysed sources share some distinct property that could possibly be related to neutrino production, the sample is analysed as a whole as well. Three of the investigated sources display a flaring state close to the neutrino event, although this is not highly unlikely among blazars. Other than this, no special properties were found in these four sources. Kolmogorov Smirnov tests were performed, to see if this sample is any different from the MOJAVE sample, which consists of over 300 blazars and therefore should be a fair representation of all observable blazars. The statistical tests did not reveal any significant peculiarities of these four sources, as compared to the MOJAVE blazars.

Zusammenfassung

Aktive Galaxienkerne gehören zu den außergewöhnlichsten und hellsten Objekten in der modernen Astrophysik. Im optischen Spektralbereich kann das Zentrum dieser Galaxien eine Leuchtkraft haben, die von derselben Größenordnung ist wie der Rest der Galaxie. Sie sind in fast allen Wellenlängen sichtbar und können einen zweiseitigen Fluss aus heißem Plasma, die sogenannten Jets, erzeugen, die teilweise größer sind als die Galaxie selbst. Solche Jets werden mit der Technik Very Long Baseline Interferometry im Radiobereich beobachtet. Diese Methode verwendet mehrere Radioteleskope, um hoch aufgelöste Bilder von astrophysikalischen Quellen zu erstellen. Somit ist es möglich, aktive Galaxienkerne, die häufig eine höhere Rotverschiebung als 0,1 haben, auf wenige Parsec aufzulösen. Im Spezialfall, dass der Jet direkt auf den Beobachter zeigt, werden diese Quellen als Blazare bezeichnet. Bisher sind Blazare die hellsten, bekannten astrophysikalischen Objekte mit einem relativ konstanten Fluss.

Neutrinos sind Elementarteilchen aus dem Standartmodell. Sie sind sehr schwer nachzuweisen und können in jedem Streuprozess entstehen, bei dem die schwache Kernkraft wirkt. Seit 2010 beobachtet das IceCube Teleskop astrophysikalische Neutrinos. Neben der Sonne und der Supernova 1987A erzeugt auch der Myonenzerfall in der Atmosphäre Neutrinos. Allerdings ist bis heute nicht zweifelsfrei klar, woher hochenergetische Neutrinos kommen.

Bereits in den 1990er Jahren wurde bereits postuliert, dass aktive Galaxienkerne, und besonders die Unterklasse der Blazare, Neutrinos mit Energien über 10 TeV produzieren. Die Messung des Neutrinos IC-170922A war einer der ersten experimentellen Hinweise, die diese Theorie mit hoher Sicherheit stützt. Es wurde in der Nähe des Blazars TXS 0506+056 gefunden. Die IceCube Kollaboration stellt daher eine Assoziation zwischen diesen zwei Ereignissen her, mit einer Sicherheit von 3σ. Daraufhin wurde nach weiteren aktiven Galaxienkernen gesucht, die nahe an der Position eines hochenergetischen Neutrinoevents liegen.

Vier dieser potenziellen Neutrino Quellen, TXS 0506+056, PKS 0723-008, 4C +06.41 und PKS 1502+106 werden in dieser Arbeit behandelt. Dabei wird deren Radiospektrum analysiert, um herauszufinden, ob sie ungewöhnliche Eigenschaften besitzen, die mit der Produktion hochenergetischer Neutrinos zu tun haben könnten. Die Quellen sind analysiert hinsichtlich ihrer Flussdichte, Kinematik, Morphologie und Polarisation. Allerdings zeigt keine von ihnen nennenswerte Auffälligkeiten. Zum Vergleich werden die Blazare aus dem MOJAVE sample verwendet. Nur 1502+106 ist ein relativ heller „Flat Spectrum Radio Quasar“ mit einer hohen Jet Geschwindigkeit.

Um herauszufinden, ob diese vier Quellen eine bestimmte Eigenschaft gemeinsam haben, die mit der Produktion eines Neutrinos zusammenhängen könnte, wurde das Sample als Ganzes analysiert. Drei der vier Blazare befanden sich in einer Phase steigender Helligkeit, als das Neutrino gemessen wurde, was allerdings bei Blazaren nicht sehr ungewöhnlich ist. Davon abgesehen gab es keine Auffälligkeiten in diesen vier Quellen. Es wurden Tests nach Kolmogorov Smirnov durchgeführt, um Unterschiede zwischen diesem und dem MOJAVE sample zu finden, wobei letzteres aus über 300 Blazaren besteht und damit die Allgemeinheit aller Blazare gut repräsentiert. Diese statistischen Tests besagen, dass die vier Quellen keinerlei Auffälligkeiten aufweisen, wenn sie mit dem MOJAVE sample verglichen werden.

Contents

1 Motivation

Source identification is a challenge often occurring in multi-wavelength astronomy. Observations are generally made in only a certain section of the electromagnetic spectrum, like the radio, optical, X-ray and γ-ray regime. Due to their different wavelengths, different methods are used for observation, and usually different teams operate these observations. Therefore, it is not uncommon that one astrophysical object is known by multiple names which originate from different catalogues. To confirm that the emission detected in two observations has been produced by the same source, multiple criteria have to be met. Probably the most obvious and important of these criteria is, that the radiation must originate from the same spot or area in the sky. However, there are other criteria that have to be fulfilled, because it is possible that two observable objects are located in the same area in the sky but cannot be resolved as two sources.

Source identification is an issue in neutrino astronomy as well. Neutrinos only interact with gravitation and the weak nuclear force, so a neutrino detector relies on the rare random event of them scattering into traceable particles, like e.g. muons, inside the telescope. Therefore, only relatively few have been found, and their statistical implication is rather imprecise. Telescopes like, e.g. the *Fermi*-LAT (large area telescope, Abdo et al. 2009), deliver a lot of data, so it is easy to distinguish the background radiation from actual γ-ray sources. Contrary, neutrino observatories like the IceCube Neutrino Telescope (IceCube, IceCube Coll. 2006) or the Super-Kamiokande detector (Fukuda et al. 2003) have a lot less detections to work with, especially in the high-energy regime. As a result, only two objects, that are known from their electromagnetic radiation, the sun and the supernovae 1987A, have been identified to also emit neutrinos (see e.g. Katz & Spiering 2012). Every other neutrino observation to date could not be related to a known object with a sufficiently high confidence level.

Still, there are multiple papers pointing out that a certain source could likely be the origin of a measured neutrino. Most notably, the paper by the IceCube Collaboration (2018) claims that the blazar (see Sect. 3.1 Blazars) TXS 0506+056 is a highly likely source for the neutrino event IC-170922A. This would not only imply that some AGN (Active galactic nucleus, see Sect. 3) emit neutrinos, but also suggest, that high-energy neutrinos are at least in part extragalactic. A highly confident association between a blazar and a high-energy neutrino would therefore be a ground-breaking discovery. The neutrino IC-170922A and its AGN counterpart have the highest confidence level of an association (3σ, IceCube Coll. 2018) among neutrinos with energies over 10^{13} eV so far. However, there are other extragalactic sources in spatial coincidence with a known astrophysical neutrino event. Some of them, a small sample of blazars, is given in Table 1.

Neutrino Reference	Coincident source	Date
ID 5 (Aartsen et al. 2014)	PKS 0723-008	12.11.2010
ID 63 (IceCube Coll. 2017) / IC-141209A	4C +06.41	09.12.2014
IC-170922A (IceCube Coll. 2018)	TXS 0506+056	22.09.2017
IC-190730A (Taboada et al. 2019)	PKS 1502+106	30.07.2019

Table 1: For these neutrino events, there are AGN that are possible candidates for their creation. All of them classify as track-type events. The apparent sources are blazars and have been subject of multiple publications. The date gives the time when the neutrinos were measured by the IceCube observatory.

This thesis is not supposed to prove whether the selected apparent sources emit neutrinos. These four blazars, TXS 0506+056, PKS 0723-008, 4C +06.41 and PKS 1502+106, all lie within areas where a high-energy neutrino was found. Therefore, they have already been proposed as neutrino-emitting sources in different papers (e.g. Kun et al. 2019, Garrappa et al. 2019).
The motivation of this thesis is to analyse, whether the radio properties of these four sources somehow differ from other known blazars. The MOJAVE (Monitoring Of Jets in Active galactic nuclei wit VLBA Experiments[1]) sample of blazars will be used for comparison. It is sufficiently large, has been observed for quite a long time and also contains TXS 0506+056, PKS 0723-008, 4C +06.41 and PKS 1502+106. Multiple criteria like brightness, morphology, kinematics and polarisation are prominent numeric features of a blazar, that are investigated statistically.

[1]https://www.physics.purdue.edu/MOJAVE/

2 Neutrino astronomy

Neutrinos are elementary particles that are part of the Standard Model. These Fermions belong to the family of leptons, so they play a role in the conservation of the lepton flavour. Their existence was first proposed by Pauli in 1930 to explain the energy conservation within the beta decay. Neutrinos only interact with the weak nuclear force and gravitation, which is why they are very hard to detect. However, a whole branch of astronomy has set out to find these elementary particles. Nowadays there are multiple neutrino observatories like IceCube that can trace back neutrino trajectories and their energies by observing secondary particles.
Neutrinos are generally produced in a scattering process of elementary particles. In these processes, all created particles move, so that the momentum is conserved. Due to their low mass, neutrinos contribute only little momentum and are therefore scattered almost completely into random directions. Therefore, it is reasonable to assume, that an object's neutrino flux density is emitted isotropically. However, if neutrinos were created in a relativistic jet of an AGN (see Sect. 3), their flux density would be boosted in the direction of motion, analogue to the Doppler Boosting (see Sect. 3.2 Eq. 6, Lind & Blandford 1985) of radiation, emitted by electromagnetic particles.
Since its launch in 2010, IceCube has found only a couple dozen neutrinos with an energy of a few hundred TeV [2]. These events can be categorised into shower- and track-events. Within a shower-event, the neutrino scatters into multiple other light elementary particles and its former trajectory can be approximated. In a track- or line-event, only one muon is created, limiting the region from which the neutrino could have originated to a few deg^2. This area in the sky generally cannot be described by any simple shape. However, for simplicity, it is usually approximated to be elliptic. There is no numeric limit between track- and shower-type events, but the traces in the detector define which event has occurred. Four high-energy neutrino events measured by IceCube will be analysed in this thesis.
The first of these four neutrinos was measured on 12.11.2010. It was published by Aartsen et al. (2014) under the name ID 5. The neutrino was found at the position $R.A.: 110.6°$; $Dec.: -0.4$ (07h 19m 51s, -00d 18m 13s in B1950 coordinates) with a median angular error that is smaller than 1.2 degrees (Aartsen et al. 2014). The elliptical area the neutrino likely originated from is small enough to conclude that it started a track-type event. Its energy is 71.4 ± 9.0 TeV.
The second neutrino event, IC-141209A, was made public as ID 63 by the IceCube collaboration (IceCube Coll. 2017). Its position is $R.A.: 160.0°$; $Dec.: 6.5°$ (10h 37m 24s, 05d 51m 40s in B1950 coordinates) and it struck the detectors on 09.12.2014. The upper limit of the angular position error is 1.2 degrees and the neutrinos energy is 97.4 ± 9.6 TeV.
The most recent neutrino event was not included in any refereed publication yet. However, it was subject to multiple ATel (Astronomer's Telegram[3]) reports. Taboada et al. (2019, ATel 12967) presented the high-energy neutrino event IC-190730A which was found by IceCube on 30.07.2019. Its coordinates are $R.A.: 225.79°$; $Dec.: 10.47°$ (15h 00m 45s, 10d 39m 55s in B1950 coordinates). The error is given in the form of a 90% containment area which has a maximum radius of 1.43 degrees. Therefore, it is also classified as a track-type event. The neutrino's energy is already listed in its GCN (Gamma-ray Coordinates Network[4]) report with 298.8 TeV.
The most prominent of the four events is the discovery of the high-energy neutrino IC-170922A that was registered by IceCube on 22.09.2017. Its coordinates are $R.A.: 77.43°$; $Dec.: 5.72°$

[2]Interpolation with the neutrino events from Aartsen et al. 2014 and IceCube Coll. 2017
[3]http://www.astronomerstelegram.org/
[4]https://gcn.gsfc.nasa.gov/

(05h 07m 03s, 05d 39m 28s in B1950 coordinates) with a 90% containment area that reaches out only 0.95 degrees at maximum. Its energy was computed to be 290 TeV with a 90% containment error reaching to 183 TeV. Multiple papers have been issued concerning this detection. The first publication of the neutrino (IceCube Coll. 2018), that included all of the previously mentioned data about IC-170922A, focused on only this one event because it had a major implication. The paper gives a 3σ confidence association between IC-170922A and the flaring of the blazar TXS 0506+056 (see Sect. 5.3.1). A probability this high is extremely rare in neutrino astronomy, and results from the fact that numerous neutrino events at lower energies have been found in the same region in the sky. This paper from the IceCube Collaboration suggests that a whole class of astrophysical objects, the AGN, could be emitting high-energy neutrinos. This theory is not new. The production of high-energy neutrinos in AGN was already proposed in several paper (for example Mannheim 1993 and Mannheim 1995). An association of IC-170922 and TXS 0506+056 would provide the first observational evidence regarding this theory.
Its energy is a good indicator of where a neutrino likely originated from. Models predict that each class of neutrino-emitting sources produces its own energy distribution (e.g. Katz & Spiering 2012). Most of the observed neutrinos are cosmological neutrinos, solar neutrinos, or

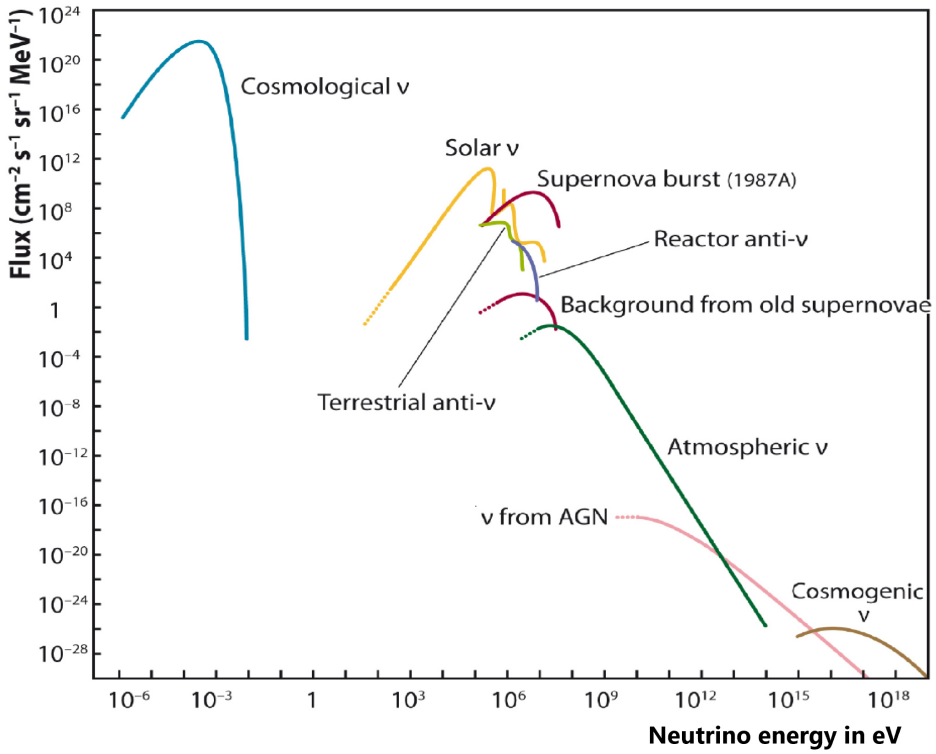

Figure 1: The neutrino energy distribution is mostly based on theoretical models. It represents the kind of source, a neutrino with a specific energy likely originated from. Even though the flux density of, e.g. solar neutrinos is well known, too few high-energy neutrinos have been measured so far to determine their sources, or even source-type, with certainty.
source: Katz & Spiering 2012

are produced in supernovae. Neutrinos with energies over 10^9 eV are mostly created within particle decay processes in the atmosphere, e.g. the muon decay. Due to the steep spectrum within this distribution, it is reasonable to assume that neutrinos with energies over 10^{15} eV

do not originate from any of those previous sources. Since they must be emitted from a very high-energy object, Katz & Spiering (2012) also propose that neutrinos with energies over 1 PeV could be produced in an Active Galactic Nucleus (AGN, see Sect. 3), a gamma ray burst (GRB), or a Starburst Galaxy. However, due to its short duration, the chances of finding a neutrino from a GRB are relatively small. An association of a neutrino event with an AGN would not only confirm this theory and be another confirmed source of neutrinos but could also reveal information about the processes that take place within an AGN. The observation of IC-170922A in spatial coincidence with TXS 0506+056 and a 3σ confidence level for an association is one of the most likely associations made in high-energy neutrino astronomy so far.
However, since to date so few neutrino observations have been made in this energy band, their statistical implication has to be treated with care. Additionally, so far it is only a theory, that these high-energy neutrinos originate from an extragalactic source. It is not highly unlikely for neutrinos with energies like ID 5 or ID 63 / IC-141209A to originate from decay processes in the atmosphere (Aartsen et al. 2014).
Also, it should be noted that not all AGN are alike. There are several different classes (see Sect. 3), and associating one AGN with a neutrino event does not necessarily imply that all of them emit neutrinos.

3 AGN

Active galactic nuclei (AGN) were first described as a class by Carl Seyfert. He found galactic nebulae, mostly elliptic galaxies, with a dense region within their bulge that emitted a large percentage of the whole galactic luminosity (Seyfert 1943). This kind of emission does not result from nuclear fission but from a different kind of energy source. Salpeter was one of the first to propose that an accretion process of matter onto a very dense object could emit high levels of energy in the form of radiation (Salpeter 1964). Nowadays, we assume that this dense object is a supermassive black hole (SMBH) that is likely to be found in the center of every galaxy. If this SMBH accretes $\approx 1 M_{\odot}$ per year, a luminosity up to $L \approx 10^{10}\, L_{\odot}$ ca be emitted from the innermost region of the galactic bulge and the source is called an active galaxy or AGN. This brightness can vary strongly, depending on the source. From approximations of an AGN spectrum the total energy output, among all wavelengths, can be estimated. This bolometric luminosity lies somewhere between $10^{40} \frac{\text{erg}}{\text{s}}$ for faint sources and $10^{49} \frac{\text{erg}}{\text{s}}$ in especially bright sources (Beckmann & Shrader 2012). Multiple kinds of AGN were found, which made a categorisation necessary. However, most of these classes are not clearly separated from another, and there are a lot of sources that cannot be classified distinctly.
The main characteristics that differ within AGN are the radio loudness, the spectrum, and the luminosity. About 85% of all AGN are radio-quiet sources (Kellermann et al. 1989), which means their radio flux density is approximately as high as their flux density in the optical spectrum ($R_{r-o} \approx 1$). On the other hand, radio-loud sources have $R_{r-o} \geq 10$.

$$R_{r-o} = F(6\text{GHz})/F(4400\mathring{A}) \tag{1}$$

According to the standard model of AGN, radio loudness can be related to the formation of a highly collimated outflow of plasma, originating somewhere close to the accretion disk. This flux of particles with relativistic velocities is called a jet. Some of these jets exceed their host galaxies in size and some are visible among frequencies from the lower radio regime to γ-rays.
The total brightness is an indicator of the kind of AGN a source can be associated with. Bright but radio-quiet sources are called Quasi Stellar Objects (QSOs), while less bright sources are called Seyfert galaxies. Both classes are further subdivided according to their spectrum. If broad and narrow emission lines are found, the sources are called QSO 1 or Seyfert 1 AGN. If only the narrow lines are found, they are called QSO 2 or Seyfert 2 AGN. Broad emission lines usually indicate a rotation at high speed, so that the emission is altered due to the Doppler effect.
The distinction between broad and narrow lines is also used with the radio-loud AGN. In these sources, the differentiation is made between Broad Line Radio Galaxies (BLRGs) and Narrow Line Radio Galaxies (NLRGs). However, radio-loud AGN can also be classified by the kind of radio morphology they show. The degree of collimation of the jet, as well as its size and form, can vary from one AGN to the other, so that it is useful to sub-categorise them further. There are jets that become fainter, the further they extend out from the central engine. The corresponding AGN have been classified as Fanaroff-Riley 1 sources. On the other hand, there are radio-loud AGN that have a relatively high collimated jet, with a radio lobe at its end, that can be even brighter than the core. These objects are called Fanaroff-Riley 2 sources (Fanaroff & Riley 1974).

3.1 Blazars

Another class of radio-loud galaxies are blazars. Even though they are radio-loud, no extended jet can be found when observing them on kpc-scales. Their spectrum $F(\nu)$ is relatively flat in the GHz regime and usually has only very narrow emission lines in the optical spectrum. Generally, they are brighter than other AGN, and their flux can be highly variable, sometimes even within only a few days. Furthermore, their emission can be highly polarised (up to 15%, Hodge et al. 2018).
There are two types of blazars, the BL Lac objects, named after their sub-classes prototype BL Lacertae and the Flat spectrum Radio Quasars (FSRQs). The latter subclass of blazars is more luminous and also shows more emission lines in their optical spectrum, which is why they are associated with Quasars (quasi-stellar objects). Statistical analysis shows that FSRQs show significantly higher jet speeds and also have different polarisation properties than BL Lacs (Zensus 1997).
When observing them on arcsecond-scales, most blazars show none, or only very few extended features. By resolving the AGN further, their structure can be revealed. They usually show signs of a jet on milliarcsecond (mas) scales, consisting of one or more bright features moving away from the core.
The radio-band emission of a blazar is dominated by synchrotron radiation (Zensus 1997) originating in the jet. Their radio spectrum is often approximated by a power law:

$$S_\nu = \nu^\alpha. \tag{2}$$

Here α is the spectral index, with values typically around -1 for extended emission regions.
This characteristic, observed behaviour can be understood by assuming, that the energy distribution of electrons in an AGN component follows E^{-p} (Rybicki & Lightman 1979). One emission region, containing particles that emit synchrotron radiation, exhibits a peaked spectrum. For compact components the spectrum's maximum is dependent on the component's optical depth, its flank towards higher frequencies has an $\alpha \approx -1$.
A blazar, that is composed of multiple features, stacks the spectral curves of all its components. The resulting radio spectrum is usually flat with $\alpha \approx 0$.
Over the whole spectrum, from radio to γ-rays, the spectral energy distribution (SED) of most blazars is decreasing continuously (see e.g. Türler et al. 1999). When plotting νS_ν the function basically describes the power that is emitted in a certain wavelength interval $d\nu$. Here a bimodal distribution can be found in most blazars (double hump structure see Fig. 2). The left of these two maxima is believed to originate from synchrotron radiation. There are multiple theories aiming to explain the origin of the high-energy hump. They usually assume hadronic and lepto-hadronic scattering or, e.g. the synchrotron self-Compton effect to produce high-energy photons (Beckmann & Shrader 2012).

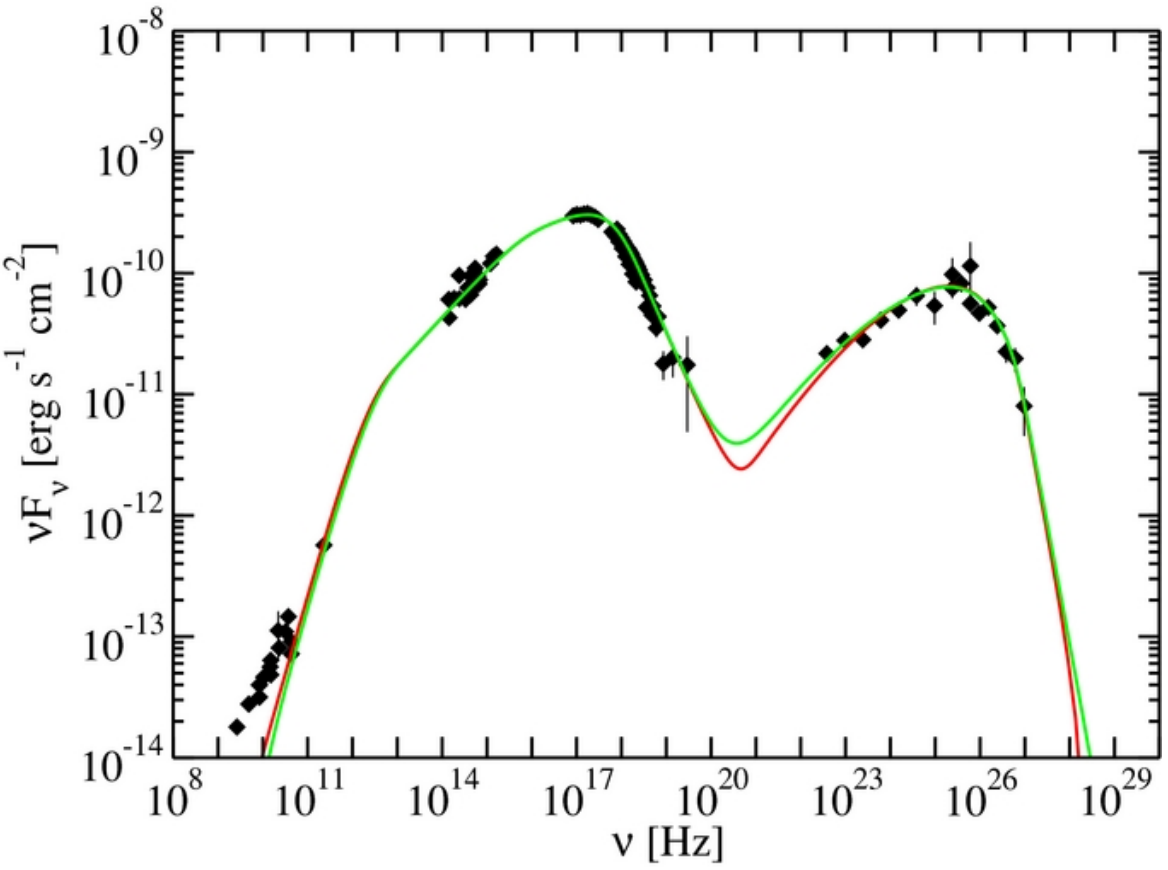

Figure 2: $\nu\, S_\nu$ of the blazar Mrk 421. In this graph one can see the typical double hump structure of a blazars power emission distribution fitted to the measured data.
source: Abdo et al. 2011

3.2 Unification model

Urry and Padovani (1995) describe the generally accepted unification model that aims to explain why there are so many variants of AGN. Their approach suggests, that all AGN observations can be explained by varying the viewing angle towards the same kind of source (see Fig. 3). The inherent differences in all classes of active galaxies are, how luninous the source is and whether it is radio-loud or radio-quiet. All other observational properties can be explained with the viewing angle towards the AGN's rotation axis.
At the center of the AGN, there is the SMBH. Its mass can vary between approximately $10^5\, M_\odot$ and $10^{10}\, M_\odot$ (Beckmann & Shrader 2012). The accretion disc, composed of hot, radiating plasma, is rotating around it. Matter from this region can be accreted onto the SMBH and thereby release energy at a rate, that can not be explained by any other known process, like e.g. nuclear fission. This whole system is surrounded by a torus (dusty absorber in Fig. 3) and many clouds of gas.
The broad lines occurring in Sy 1, QSO 1 and BLRG as well as the narrow lines in Sy2, QSO 2 and NLRG can be explained with a Doppler shift. In the sources that show broad and narrow lines, the observer can see the center of the AGN. There, the clouds of material spin around the SMBH with very high velocity and therefore emit emission lines that are evenly shifted to smaller and bigger wavelengths. When observing the whole system, these lines appear as if they were one broad line. In sources where only narrow emission lines are found, this innermost

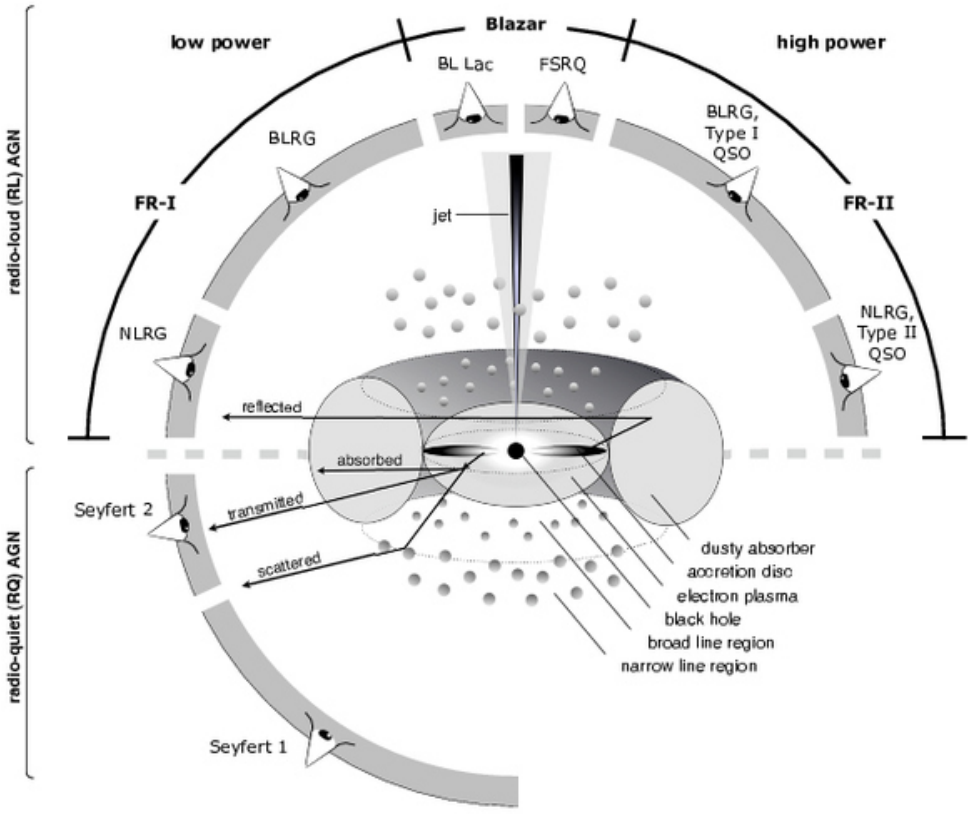

Figure 3: This graphic is a visualisation of the unification model by Urry and Padovani (1995). There are radio-quiet (lower half) and radio-loud (upper half) AGN. The latter can be divided into high (top right) and low (top left) power sources. Depending on these intrinsic properties and the angle of observation, the AGN are classified differently.
source: Beckmann and Shrader 2012

region is shielded from observation by the torus. Only the material in the narrow line region can be observed, which spins around the central engine much slower.
In blazars, the jet extends very closely to the line of sight. Therefore, it usually seems as if the jet is much shorter than in other AGN and can only be seen with sufficient angular resolution. In the majority of all blazars it seems as if some of its jet features move away from the core with superluminal motion (see e.g. Lister et al. 2019). This is due to a projection effect (see Fig. 4). A bulge of radiating material, often called a "blob", is likely travelling towards the observer at a speed v that is close to c. For simplicity, we assume the blob is constantly emitting radiation isotropically. From the observers position the blob moved the distance

$$s \;=\; (t_1 - t_2) \cdot v\, sin(\Phi). \tag{3}$$

When emitting the photons at t_2, the plasma is closer to the observer than it was at t_1. Therefore, the time difference between receiving the photons from t_1 and t_2 is

$$\Delta t \;=\; (t_2 - t_1)(1 - \frac{v\, cos(\Phi)}{c}). \tag{4}$$

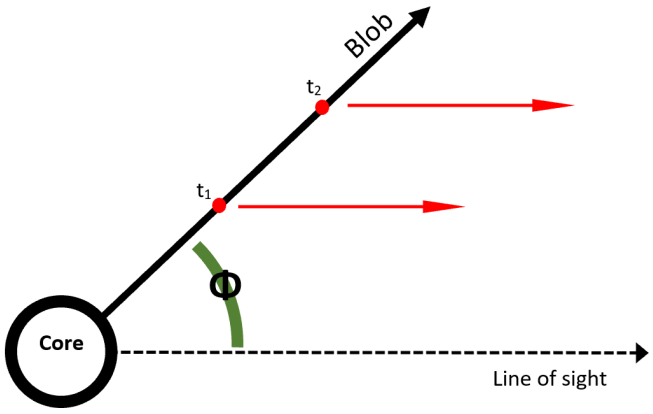

Figure 4: Many blazars show apparent superluminal motion. The projection effect causing this motion can be explained with a small angle Φ between the line of sight and the direction of the relativistic motion of the blob. The apparent motion of the jet component in the plane of the sky can be computed with the Eq. 3 to 5.

The apparent motion in the plane of the sky therefore has an apparent speed

$$v_{app} = \frac{v\, sin(\Phi)}{1 - \frac{v}{c} cos(\Phi)}. \tag{5}$$

v_{app} can exceed c, and so it is possible that $\beta_{app} = \frac{v_{app}}{c}$ is greater than 1. Blazars are defined to having a small Φ, and it is not uncommon that the jet speed v is highly relativistic. These properties favour $\beta_{app} \geq 1$ which is why so many of this AGN-type show apparent superluminal motion.
The fact that the radiating plasma is moving towards the observer with a high β, also initiates the so-called "Doppler boosting" (Lind & Blandford 1985). It is due to a relativistic effect that results from the Larmor formula (Eq. 6) and can be derived from the Lorentz invariance.

$$\frac{dP}{d\Omega} \propto \frac{|\vec{n} \times ((\vec{n} - \vec{\beta}) \times \dot{\vec{\beta}})|^2}{(1 - \vec{n} \cdot \vec{\beta})^5} \tag{6}$$

Here dP is the power radiated towards the observer, located in the direction of $\vec{n}$, per solid angle $d\Omega$.
Consider a particle that is radiating a constant, isotropic flux density in its rest frame. If this particle is observed at a relativistic speed, with a Lorentz factor $\gamma = \sqrt{1 - \beta^2}^{-1} >> 1$, its emission no longer appears to be isotropic. The Larmor formula describes how much of its emitted flux is radiated in which direction.
For example, this effect can occur when an excited electron is moving towards the observer at a high speed. Its radiation will appear much brighter, because most photons are emitted along the direction of travel. A high percentage of these photons are being collimated into a cone with an opening angle of $\frac{1}{\gamma} = \sqrt{1 - \beta^2}$ in the direction of motion.

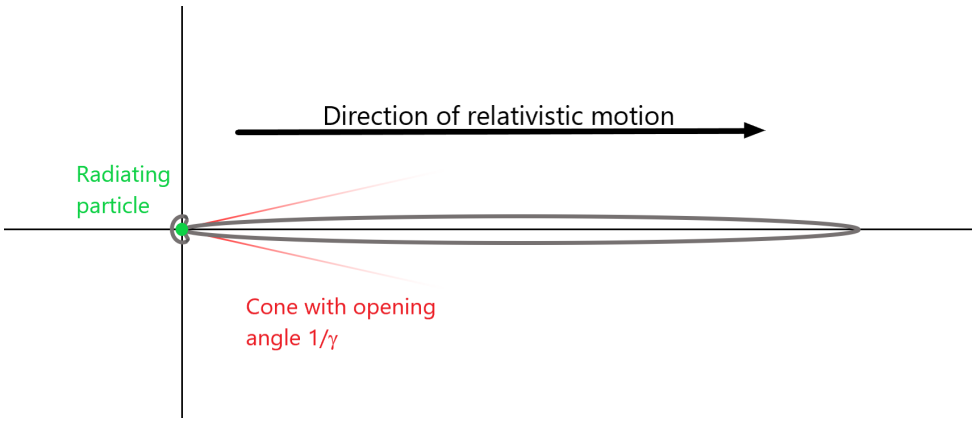

Figure 5: Visualisation of Doppler boosting. In the observer frame, a particle (green), with a velocity close to c, emits the majority of its radiation into a small cone (red). The opening angle of the cone is $\frac{1}{\gamma}$, and its axis is aligned with the direction of motion. A relativistic electron, e.g. would radiate most photons at a small angle to the direction of travel.

In a blazar, where radiating plasma is travelling towards the observer, this Doppler boosting will cause the emission of a blob to appear much brighter than it would in its rest frame. This is why blazars often seem to be more luminous than other AGN. Therefore, they can be found at much larger distances what offers a much larger space where they can be found. This is why, even though the alignment of jet and line of sight is generally very unlikely, a substantial number of blazars has been found, when compared to the number of other AGN.

4 Parsec scale radio jets

4.1 Very long baseline interferometry

AGN can be found in many different wavelength bands. Their emission reaches from the highest energies in the γ-ray band to the lower radio frequencies. Vapour in the troposphere can interfere with radiation with a frequency above $\approx$ 100 GHz, and particles in the ionosphere can distort the beam if its frequency is lower than $\approx$ 200 MHz (see e.g. Wootten et al. 2009). This leaves the so-called radio window, a band of wavelengths in which the radio waves are not majorly hindered from passing through the atmosphere.
When performing radio observations, the angular resolution Γ is a crucial factor. It is a lower limit for the distance two observed objects can have, to still be perceived as separate objects. For better resolution it is crucial, that Γ is as small as possible. It can be calculated with the Rayleigh criterion.

$$\Gamma = arcsin(1.22 \cdot \frac{\lambda}{d}) \tag{7}$$

Here, λ is the wavelength and d is the diameter of the telescope. To reach resolutions of a few parsec in AGN, which usually have redshifts with a magnitude of 0.1 (Lister et al. 2019), Γ has to be as small as only a few mas. To reach this at long radio wavelengths, a telescope with a diameter of hundreds of kilometres would be required.
This problem can be solved with radio interferometry (Kellermann & Moran 2001). An array of telescopes is used to observe the same source by synchronising their observational data. Therefore, the parameter d in the Rayleigh criterion is shifted to the longest distance between two telescopes, called the baseline. This technique is called very long baseline interferometry (VLBI). It is used in multiple instruments, like e.g. the very large array (VLA, Kassim et al. 1993), the low frequency array (LOFAR, van Haarlem et al. 2013) or the very long baseline array (VLBA, Napier 1994).
To reassemble the observational data from all telescopes into one image, it is synchronised in a correlator, and then further analysed with the software Difmap (Shepherd et al. 1994). Within this imaging process the measured fringe visibility is analysed with the CLEAN algorithm (Högbom 1974). This algorithm relies on the following loop. First, the brightness distribution of a source is separated into many point-shaped sources. The brightest ones are treated like a feature of the AGN. They are added to the "clean image" in the form of an elliptical Gaussian feature, and subtracted from the measured brightness distribution. After several recursions, until a certain flux density limit, the clean image will ideally contain the bright features of the AGN without the side maxima of the fringe visibility. These bright features are called components and have a position, a size, an axis position angle and a certain flux density. A component contained in a jet is sometimes also called a blob. Almost all VLBI images of AGN are composed of one main component, usually one or more side components, and the background noise.
With the arrangement of the side components, relative to the core, the morphology of the source can be modelled. By observing the same AGN at different times, the so-called epochs, its time development can be investigated. This is especially interesting, because the motion of components in a jet could provide information about its creation. The background noise reveals the quality of the image. If the background shows periodic or symmetric shapes that surpass other features in brightness, it is very likely that an error occurred during the imaging process, more specifically in the self calibration.

4.2 MOJAVE

The MOJAVE program is a long-time observation project that is investigating the radio properties of AGN. It was launched in 1994 and uses the VLBA telescopes to investigate primarily blazars at a wavelength of 2 cm. The general aim of the program is to understand how a jet forms, how matter is moving and radiating within the jet, and finally, how an AGN radio spectrum is related to other wavelengths. Due to the long time-span of observation, the temporal development, especially the motion of distinct features, can be analysed in the observed AGN. Multiple papers have been published by the association. The complete MOJAVE archive of all their sources and observations is available on their website[5].

The number of observed sources has increased during the time of MOJAVEs existence. In their first publication (Kellermann et al. 1998) already 132 sources were included, although the project was not called MOJAVE yet. In their paper, the MOJAVE team first presented their criteria for a source to be included in their catalogue. All sources must be AGN and have a radio spectrum that is flat above 500 MHz. In this case, flat was defined as the spectral index α, from the fitted power law $S \propto \nu^{\alpha}$, being larger than -0.5. Also the total flux density at 15 GHz had to exceed 1.5 Jy in the northern sky and 2 Jy in between the celestial equator and a declination of $-20°$. A few exceptions were made by including some sources, even if they didn't fulfil these requirements, or by excluding some, that did meet the criteria. Sources that were e.g. gravitationally lensed were excluded.

The program was continued under the name MOJAVE from 2003 on. In the paper Lister et al. 2009, the "Original MOJAVE" sample was introduced. It included 135 sources and differed from the previous sample by only one criterion. The sources had to exceed the flux density limit of 1.5 Jy (or 2 Jy for sources in the southern sky) in only one epoch of their observation between 1994 and 2004.

The sample was enlarged to a size of 180 sources with the introduction of the "Original MOJAVE 1.5 Jy" sample in Lister et al. 2013. In this set of AGN, the radio spectra above 500 MHz are also flat, however all sources with a declination $\geq -30°$ that surpassed 1.5 Jy in any epoch from 1994 until 2010 were included. Still, a small number of exceptions were made to include or exclude a few special sources. The only difference in the "MOJAVE 1.5 Jy Quarter-Century" sample (Lister et al. 2019) was, that the time of observation now included observations up until 2019. This sample contained 232 observed objects.

There are a few other samples that have been included in the MOJAVE observations that did not fulfil the criteria of the original samples. However, they were chosen according to other features, e.g. the "Hard Spectrum" sample or the "Low-Luminosity" sample. One of these special samples is the "*Fermi*-MOJAVE" sample which was introduced by Lister et al. 2011. It included 116 sources that are above a declination of $-30°$ and have an average integrated *Fermi*-LAT energy over 0.1 GeV in the 1FGL catalogue period.

The complete MOJAVE sample, that will be used for comparison in Sect. 5.4, contains every source, that the program ever observed. This means not only the "MOJAVE 1.5Jy Quarter-Century" sample but also all other special samples are included.

[5]http://www.physics.purdue.edu/astro/MOJAVE/

4.3 Jet models

Classical jet models (e.g. Lind & Blandford 1985) typically describe AGN jets as a flow of hot, radiating plasma. This material is ejected from a region that is called the central engine of the AGN. This is not necessarily the SMBH or the accretion disc. How and where the jet actually forms is still debated, but it is safe to assume, that it is powered by an accretion process (Zensus 1997). The shape of the jet is majorly influenced by the strong magnetic fields created by the SMBH. Many simulations have been performed to explain the creation of the jet (e.g. Nair et al. 2005). They usually use magneto-hydrodynamics because near an AGN strong magnetic fields are present and the flow of plasma has to be treated like a charged fluid.
The jet of a luminous AGN can be found in multiple bands of the electromagnetic spectrum. This is not due to the high temperature of the plasma in the jet. Many different processes, like e.g. synchrotron radiation, are taking place that emit photons. Up to date, no model could sufficiently explain all radiating processes that contribute to the whole spectrum of an AGN.

Ghisellini et al. (2005) (and Tavecchio et al. 2004) propose a jet structure that has two main parts, the spine and the sheath. The spine is a highly collimated and relativistic stream of matter within the jet. The sheath surrounds the spine like a hollow cylinder (see Fig. 6). The matter within the sheath moves along the jet much slower. It is likely that particles, in particular photons, from the sheath eventually interact with the matter in the spine. Ghisellini et al. (2005) assume that because these collisions happen on relativistic speeds the particles are boosted against each other (Doppler boosting, see Sect. 3.2). Therefore, the synchrotron and the inverse Compton radiation are enhanced radically. This model could explain why some sources are so bright in the γ-ray band, sometimes even brighter than in the radio band.

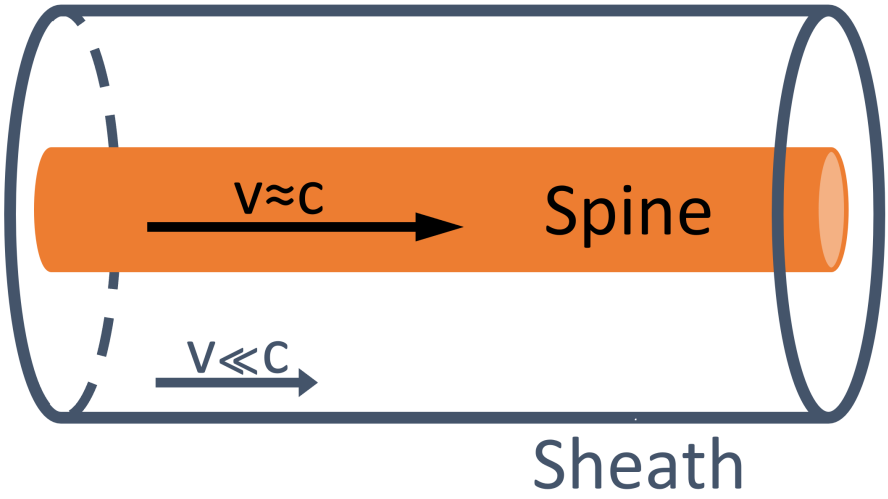

Figure 6: Jet model from Ghisellini et al. 2005. The inner layer, called the spine, is a channel in which plasma flows along the jet with highly relativistic speeds. It is surrounded by the sheath which is a less collimated outer layer of the jet. The particles in the sheath move along the jet much slower.

However, it is likely, that not only a high flux of γ-rays, but also many high-energy neutrinos are produced in these collisions (Tavecchio et al. 2014). In the rest frame of particles in the

spine is seems as if many photons from the sheath are boosted towards them with relativistic speeds. Assuming that there are hadronic particles in the jet, a photo-pion process can occur that is likely responsible for a flux density of high-energy neutrinos.

$$\pi^{\pm} + \gamma \longrightarrow \mu^{\pm} + \nu_{\mu} \longrightarrow e^{\pm} + 2\,\nu_{\mu} + \nu_{e} \tag{8}$$

In this Eq. the neutrinos and anti-neutrinos are are not treated separately, because this does not play any role in their detection. Ros et al. (2020) found signs of this spine-sheath structure in a 43 GHz VLBI observation of the blazar 0506+056. Therefore, an analysis of parsec-scale radio jets could be able to reveal properties that are unique in candidate neutrino blazars.

5 VLBI properties of four candidate neutrino blazars

5.1 Sample

The sample that is being observed in this thesis consists of the blazars in Table 2. In the following, it will be referred to as the MOJAVE-IceCube (MIC) sample, because the four sources are included in the MOJAVE program, and they are in positional coincidence with high-energy neutrinos measured by IceCube. The four sources were observed with the VLBA at 15 GHz,

B 1950 Name	Alias	optical classification	Redshift
0506+056	TXS 0506+056	BL Lac	0.337
0723-008	PKS 0723-008	BL Lac	0.127
1038+064	4C +06.41	FSRQ	1.265
1502+106	PKS 1502+106 / OR 103	FSRQ	1.838

Table 2: These are the four sources from the MIC sample. They are all part of the MOJAVE program and are therefore addressed by their B1950 name here. The aliases, the optical classification, and the redshift are taken from Lister et al. 2019

as part of the MOJAVE program in multiple epochs, even though not all of them have always fulfilled the MOJAVE sample flux density criteria. From this point on they will be referred to by their B1950 name to stick with the conventions of the MOJAVE. Their radio spectrum is flat (the power law index α is bigger than -0.5), as is usual for radio blazars. In addition, the four sources have been observed by the Owens Valley Radio Observatory (OVRO) and are known to emit radiation in the gamma regime (Hodge et al. 2018, Garrappa et al. 2019). All of them have recently been raising attention, due to each of them lying close to an area where IceCube found a high-energy track-type neutrino. These events led to the publication of several papers, that either claim that these blazars emitted the measured neutrinos or that they are possible candidates for their emission.

Apparent source	Associating paper	Neutrino Reference	MJD
0506+056	Kun et al. 2019	IC-170922A	58018.8712
0723-008	Kun et al. 2017	ID 5 (Aartsen et al. 2014)	55512.5516
1038+064	Garrappa et al. 2019	IC-141209A	57000.1431
1502+106	Taboada et al. 2019 ATel 12967	IC-190730A	58694.8685

Table 3: This Table provides an overview of which neutrino event was associated with a certain source, and also lists the paper in which this association was made. The date of the neutrino measurement by IceCube is given in the precise MJD format. The ordinary date can be found in Table 1.

The choice of these few sources could create a distorted picture, because a sample this small has only limited statistical implication. Some of the recent publications (from Table 3) were issued because these sources have been raising attention besides their spatial coincidence with the neutrino detection. It is possible that the sample is not complete and other sources near the neutrino origin, that did not show any irregular behaviour, should have been included as well (see Kun et al. 2017). The blazar 0506+056, e.g. has not only been raising attention with the possible neutrino emission, but also because it displayed a radical increase in its radio flux density. It is plausible that the IceCube detection and this flare are related, however the

possibility remains, that these two events are not correlated and therefore the association is due to a searching bias. Also it is not entirely clear, whether the four neutrinos (from Table 3) actually have an astrophysical origin, or are simply produced in the atmosphere (see Sect. 2). However, examining this sample could reveal a special observational property, that is found in these neutrino-candidate blazars.

5.2 Criteria

To test, whether the MIC sample shows any common characteristic properties, deviant from the blazar parent population, it is analysed regarding the following criteria. All the following quantities can be measured in almost every blazar that is bright enough and therefore have already been subject to a broad analysis in the MOJAVE program. Data concerning these criteria have been gathered for the complete MOJAVE sample that is assumed to be large enough to fairly represent all observable blazars (see e.g. Lister et al. 2009).

	Criterion	Numerical property	Symbol	Units
	Flux density			
a		Total flux density of the source	$F_{15\mathrm{GHz}}$	Jy
b		Flux density of the features	$S_{15\mathrm{GHz}}$	Jy
	Source morphology			
c		Compactness on arcsecond-scales	$\frac{S_{VLBA}}{S_{tot}}$	—
d		Compactness on mas-scales	$\frac{S_{unres}}{S_{VLBA}}$	—
e		Core dominance	$\frac{S_{core}}{S_{VLBA}}$	—
	Kinematics			
f		Apparent jet speed in units of c	β_{app}	—
g		Offset position and velocity angle	$\lvert P.A. - V.A. \rvert$	degrees
	Jet morphology			
h		Feature distance to the core	d	pc
i		Jet length	L	pc
j		Apparent opening angle	α_{app}	degrees
k		k-index	k	—
	Polarisation			
l		Median polarisation	m_{med}	%
m		Maximum polarisation	m_{max}	%

Table 4: All MOJAVE sources and especially the four MIC blazars are analysed regarding the criteria listed in this Table. To being able to compare these two samples, numerical properties, composed from multiple MOJAVE papers, are introduced.

5.2.1 Flux density

The total flux density of all components combined, is one of the most prominent attributes that can be measured of any source. It was recorded within every epoch of the MOJAVE program for every component of their sampled AGN (table 3 in Lister et al. 2019). For every source the flux densities of all components in one epoch were added, and then the median over all epochs was computed. This information does not show the temporal development of the blazar, and e.g. flares or the creation of a new feature cannot be found. However, in most sources the median flux density is still a good indicator of how bright a source generally is. To conduce a more precise analysis of the MIC sample, their OVRO light curves are being analysed. Blazars are known for their high variability, so a major outburst is not uncommon. However, the timing of flares or similar occurrences may show an interesting pattern among these sources.
Additionally, the median flux density over all epochs of individual jet features was calculated in Lister et al. 2019. Most jet components can be found in more than one epoch. Therefore,

the median feature flux density describes how bright single components are during the time of their observation.
This analysis was done for all sources of the MOJAVE program (not only the 1.5 Jy sample). The brightness of the sources and every feature in the MIC sample are compared to the MOJAVE sample in Sect. 5.4. Therefore, it could be possible to expose either one of the AGN or a single component as faint or bright.

5.2.2 Source morphology

The morphology of most AGN can hardly be categorised with only one parameter. Shape and size of both, core and jet, can vary. Furthermore, the form of the jet is influenced by how the single features in the jet are arranged. On their website[6], MOJAVE blazars are categorised into four classes:

- Core: Only one unresolved component (typically smaller than 0.5 mas)
- Halo: A core component surrounded by an elliptical, less luminous region
- One-sided: A core and a jet extending to one side
- Two-sided: A core, a jet extending to one direction, and its counterjet extending the other way

Since these classes are not clearly defined one can hardly use them for statistics. Therefore, the numerical quantity "compactness" was introduced by Kovalev et al. 2005. It is an attribute of the AGNs radio morphology that describes how much of the flux density is contained around the central core. A value of 1 means that the AGN can only be resolved as a point source, while a value close to 0 indicates that bright features of the source are spread over the imaging map. Because blazars can be highly variable, and the total flux density S_{tot} was measured at a different time than the other flux densities, these values can be slightly inaccurate and even exceed 1. An AGN with a bright extended jet and a relatively faint core e.g. would have a small compactness. Contrary, a brightness distribution that is dominated by a small core has a compactness close to 1. However, the compactness does not reveal all morphological properties. A circular AGN with a large core that can be resolved very well should have a small compactness, what means that circular sources do not necessarily have a high compactness. For example, a blazar with only a large halo around the radio core, and an AGN with no halo but an extended jet can not be distinguished based on this criterion.
Compactness can be subdivided into compactness on arcsecond-scales, compactness on mas-scales and core dominance. All of them are presented in Kovalev et al. 2005 (table 2) for the complete MOJAVE sample. However, 0506+056 was not included in this paper, so the compactness of this BL Lac object was computed within the imaging process for Fig. 8 (see Sect. 5.3.1).
Compactness on arcsecond-scales is the quotient of S_{VLBA} and S_{tot}. S_{tot} is the total flux density of the source, measured by a single radio telescope, while S_{VLBA} is the flux density of the components in a fully CLEANed (see Sect. 4.1) VLBA map. The CLEANed map does no longer contain the complete fringe visibility. Ideally, this algorithm removes the so-called side-lobes and only the main beam remains.
Compactness on mas-scales is the quotient of S_{unres} and S_{VLBA}. S_{unres} is the unresolved flux

[6]https://www.physics.purdue.edu/MOJAVE/

density. The visibility function gives the measured amplitude in relation to the u,v-radius where it was measured (Kellermann & Moran 2001). By only using this distribution's upper envelope (top 10%), the data of the short baselines can be neglected, so that only an unresolved image remains. The total brightness of this unresolved image is S_{unres}.
Finally, the core dominance is calculated by dividing S_{core} with S_{VLBA}. S_{core} is the brightness of the model component that represents the radio core.
For 0506+056, these values were computed according to Kovalev et al. 2005 using the visibility-data (uvf-file) from the MOJAVE website[7]. The flux densities are $S_{VLBA} = (0.530 \pm 0.026)$ Jy, $S_{core} = (0.451 \pm 0.023)$ Jy and $S_{unres} = (0,525 \pm 0.026)$ Jy, with an error of 5% as is usual for MOJAVE data (Homan et al. 2002). The single dish flux density of this blazar $S_{tot} = 0.683$ Jy was measured by the Effelsberg 100 m radio telescope (Quirrenbach et al. 1992) at 14.6 GHz on the 09.11.2017 (A. Kraus, priv. comm.).

5.2.3 Kinematics

A characteristic value of every radio-loud AGN is its jet speed. It is especially interesting in blazars, because most of their jets show superluminal motion. Bright components, called blobs, can move along the jet with velocities that seem to surpass c due to a projection effect (see Sect. 3.2). This apparent jet speed β_{app} of each component was calculated in Lister et al. 2019 (Table 4). The value of β_{app} can reach up to 40. However, the majority of components have a $\beta_{app} \leq 6$.
The direction of motion is another kinematic property of a moving feature, and therefore the VLBI jet. Most blobs move outwards radially and follow a straight, collimated jet away from the core. However, there are a few exceptions. In some jets the components don't move along the same line or don't move solely radially outwards (see e.g. Lister et al. 2019). The latter indicates that there must be some kind of acceleration within the jet. Some features even seem to move back towards the core. This motion may partially be due to projection effects, but it is obvious that the movement of blobs is not simply ballistic. The attribute of a component describing this behaviour is quantified by the offset between its position angle and its velocity angle. The position angle ($P.A.$) is defined as the angle between the NS axis and the connecting line between core and feature, the velocity angle ($V.A.$) is defined as the offset between NS and the direction of motion. The values of $|P.A. - V.A.|$ of every component in the MOJAVE sample are included in Table 4 in Lister et al. 2019.

5.2.4 Jet morphology

In addition to compactness, the structure of just the jet can also be analysed. Lister et al. (2019, Table 4) present the distance of each component from the core. The value for d is the mean of all distances in different epochs. With this information, the size of each jet can be approximated. Pushkarev et al. (2017) focused on the morphology of blazar jets. Their paper presents the quantities projected jet length L, the apparent jet opening angle α and the "k-index", describing the longitudinal shape of the jet. All these criteria were created by reading size (the FWHM of the component) and core distance of the features in the jet of 15 GHz images from multiple epochs. The projected jet length of a blazar is its maximum distance between a jet- and the core component. This value is related to d from Lister et al. 2019.
Pushkarev et al. (2017) computed the apparent opening angle by comparing size and distance

[7] https://www.physics.purdue.edu/MOJAVE/

to the core of the components in the jet. Usually, the features are aligned along a trajectory that forms the jet. In almost all cases the components, and therefore their FWHMs, are getting larger the further they are located from the core. From this distance and their diameters, the feature's individual opening angle can be determined. The median of all these angles is used as the apparent opening angle of the jet.
The k-index originates from the assumption that in a jet, the relation between diameter d and core distance r of a feature, can be described by a power law. When observing the relation in most plots, it is apparent, that there is some kind of systematic, that can often be approximated with $d(r) \propto r^k$. This means, that a jet shaped like a parabola has $k = 0.5$ and a cone would yield $k = 1$. Describing a jet with only one k-index is rather imprecise, because k can also be dependent on r. Kovalev et al. (2019) offer a more detailed analysis of the shape of jets and therefore the k-index. However, calculating a constant k for a jet is a good first approximation.

5.2.5 Polarisation

The final parameter of a blazar, that is analysed in this thesis, is the polarisation. In a jet, one of the major processes creating radiation in the radio band is synchrotron radiation. Therefore, it is not uncommon that a jet emits highly polarised radiation. Hodge et al. (2018, Table 3) calculated the percentage of polarisation in the radio cores of the MOJAVE sources in all recorded epochs. The median and maximum polarisation of the radio blazar cores were computed, and a comparison between the MIC and the complete MOJAVE sample can be found in Sect. 5.4.

5.3 Sources

In this chapter, the sources from the MIC sample are analysed individually. The OVRO lightcurves and an image of one epoch are presented for each blazar. Even though the flux density development in some of the sources show interesting behaviour, only the epochs closest to the neutrino event is imaged. This is done to avoid a searching bias. It is possible that the rise in flux density is related to the neutrino event, however this is not clearly confirmed. Therefore imaging these epochs would no longer focus on the neutrino events, but for example flares. The images Fig. 8, Fig. 10, Fig. 12 and Fig. 14 are created with visibility-data from the MOJAVE website[8], and by using natural weighting (Shepherd et al. 1994). The imaging parameters are listed in the appendix.

5.3.1 0506+056

As mentioned in Sect. 2 this BL Lac object has been raising a lot of attention recently. Not only the IceCube collaboration but also e.g. Kun et al. (2019) identified 0506+056 as a very likely source of the neutrino IC-170922A. Their spatial distance is only 0.076 degrees (or 4.6 arcminutes) which is well within the 90% confidence area of the neutrino event.
It has been observed by the VLBA since only 2009 and was introduced to the MOJAVE program with the 1FM sample from Lister et al. 2011. Due to a relatively low 15 GHz flux density of approximately 0.50 Jy in the period from 2008 to 2017, it was not included in the MOJAVE 1.5 Jy sample. The radio flux density was also measured by the OVRO (see Fig. 7), and it has shown an interesting behaviour. Since early January 2016, the flux density of the BL Lac object has been noticeably rising and is currently on its highest level since at least 2008. Therefore, Kun et al. (2019) argue that the neutrino event occurring in September 2017 gives reason to assume, that these two events are related with a high likelihood.
This blazar has been relatively faint in comparison to the MOJAVE sample. The median flux density is only 0.47 Jy even though the spectroscopic redshift is quite low ($z = 0.337$, Lister et al. 2019). As displayed in Fig. 7, the luminosity has been rising steadily since the beginning of 2016 and surpassed the mark of 1.5 Jy in May 2019. The VLBA image (see Fig. 8) reveals, that the source has a jet that is extending to the south.
The displayed epoch is the one closest to September 2017 when the associated neutrino was detected. However, this epoch did not show any unique features, that could possibly be related to enhanced neutrino emission. The single components of the jet are not aligned along a straight line. It seems as if the jet is extending to the SW at first, where it turns and is redirected towards the SE. There are multiple theories about how this shape originated.
For example, Britzen et al. (2019) propose a system of two AGN that interact with each other. The first core is supposed to be at (0,0) of the map (Fig. 8) from which its jet is extending to the south. The small bulky component, that is located near the major core to the SW, is supposed to be the second core that emits a jet to the SE.
Another possibility is, that the jet is extending to the SW at first, where it is being accelerated towards the SE. It is not unusual for a projected jet to show a bending of this extent (see Sect. 5.4). Also, the jet could be consisting of multiple components that are simply being ejected in different directions in different epochs.
An observation of the blazar at 43 GHz (Ros et al. 2020) shows an interesting behaviour. The jet shows signs of a spine-sheath structure (see Sect. 4.3). Also, this source is relatively bright

[8] www.physics.purdue.edu/astro/MOJAVE/

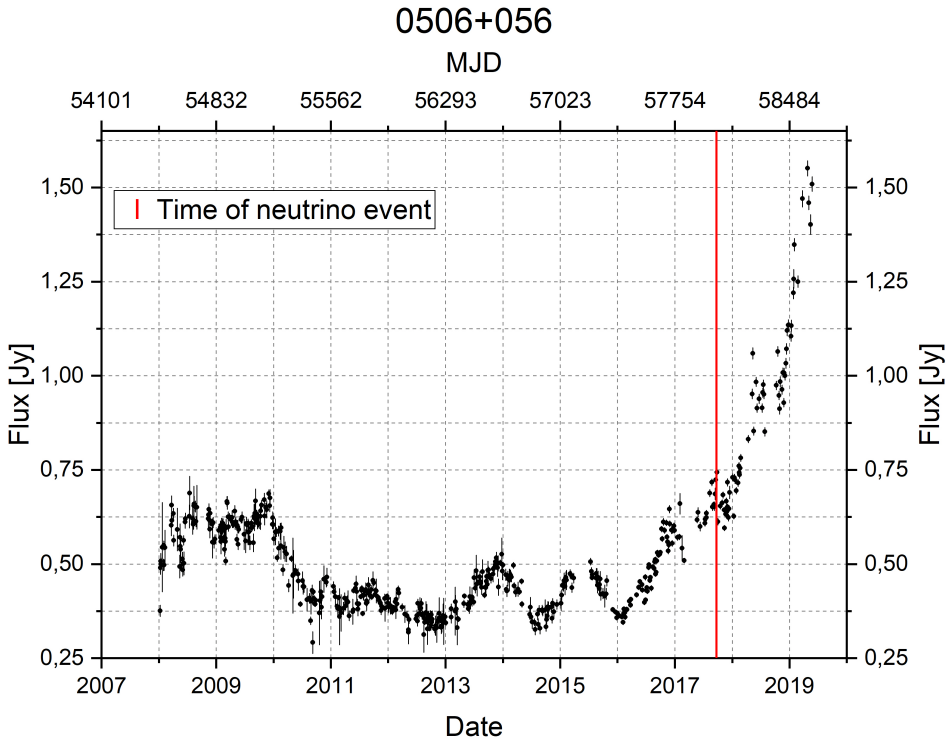

Figure 7: Total flux density of the BL Lac object 0506+056 over a 13 year span. This measurement was made by the OVRO telescope at a frequency of 15 GHz.
source: OVRO telescope website: http://www.astro.caltech.edu/ovroblazars/

in the γ-regime. This could imply that photo-pion processes, resulting from collisions within the jet, are taking place that likely enhance the high-energy neutrino flux.
When analysing the morphological parameters from Sect. 5.2.2 of 0506+056 the only property that seems to be an outlier, is the compactness on mas-scales with $\frac{S_{unres}}{S_{VLBA}} = 0.99$. The core brightness surpasses the flux density of the components easily (Lister et al. 2019). Contrary, in most MOJAVE blazars the brightness of the core is similar to the brightness of the components combined. This is mostly due to the fact that the jet features of 0506+056 are relatively faint ($S_{15\mathrm{GHz}} \leq 50$ mJy).
The compactness on arcsecond-scales ($\frac{S_{VLBA}}{S_{tot}} = 0.78$), the core dominance ($\frac{S_{core}}{S_{VLBA}} = 0.85$), the distance of the components from the core ($d < 20$), the projected jet length ($L = 35.37$), the apparent jet opening angle ($\alpha_{app} = 28°$) and the k-index ($k = 1.00$) are all within the MOJAVE average (Lister et al. 2019, Pushkarev et al. 2017).
The kinematic analysis of the components reveals that β_{app} does not surpass a value of two. The motion seems to be only mildly relativistic. However, the velocity direction of component 3 (Lister et al. 2019) shows an interesting behaviour. With an offset of 168 degrees between position- and velocity-angle, it is moving almost directly towards the radio core. This is not highly unlikely among the MOJAVE sample (see Sect. 5.4), but still remarkable.
The core polarisation of 0506+056 has a median of 1.9% and a maximum of 3.2%, which are very common values among MOJAVE blazars.

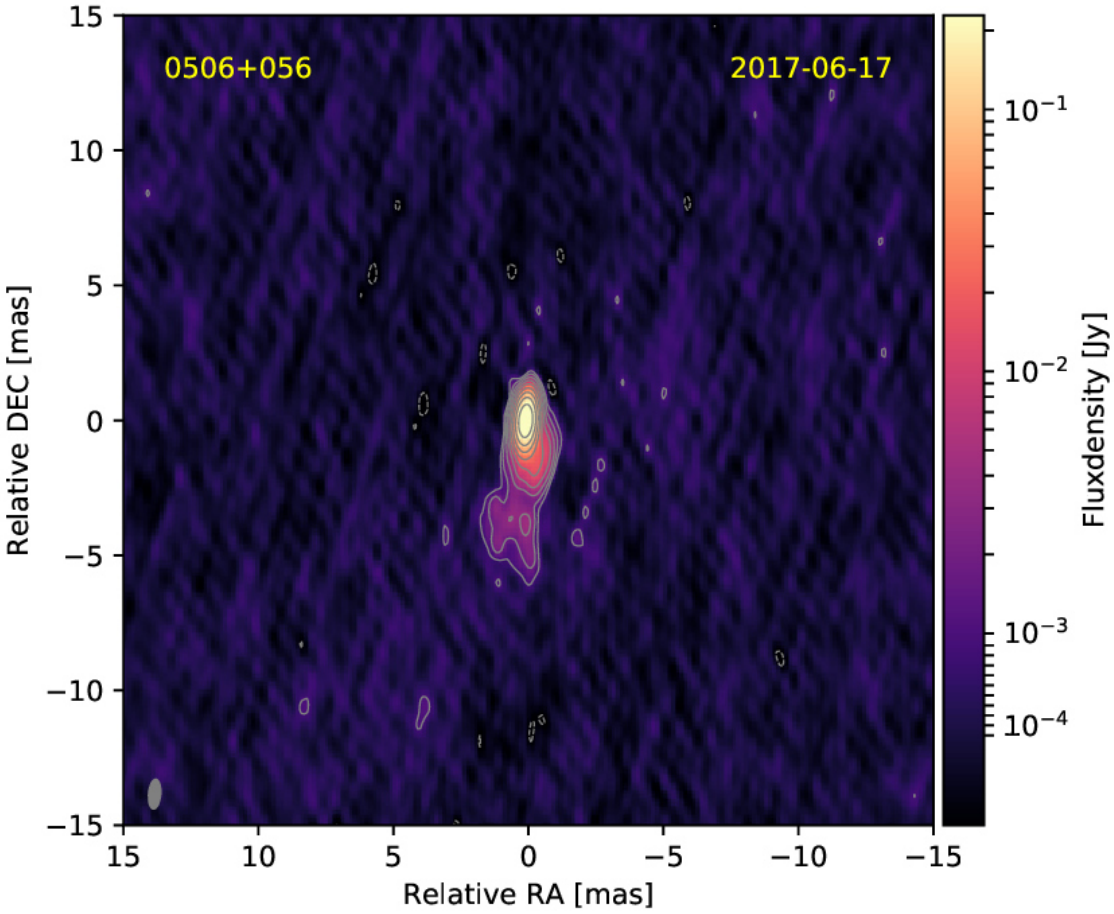

Figure 8: This 15 GHz map of 0506+056 was made with Difmap and data from the MOJAVE website. The lowest contour line is at a level of $3 \times rms$. The epoch displayed here is the one that lies closest to the neutrino event (3 months). It should be noted that the morphology of the source does not change drastically in other epochs. The full map reveals that the noise is distributed evenly, indicating that the imaging process was likely successful. The image shows a bright core and some jet components, extending towards the south.

5.3.2 0723-008

At the time of the release of Kun et al. 2017, IceCube had only found 54 extragalactic neutrinos, 14 of them were track-type events. In their paper, they claim that the BL Lac object 0723-008 likely is the emitter of the high-energy neutrino ID 5 that was found in November 2010 (Aartsen et al. 2014). This event and the blazar are only separated by 1.00 degree (60.2 arcminutes) in the plane of the sky while the neutrinos position error is limited to 1.2 degrees.
0723-008 became a member of the Original MOJAVE 1.5 Jy sample introduced by Lister et al. 2013. VLBA observations of 0723-008 from 1997 until the end of 2012 reveal that this source displayed a stable flux density at ≈ 1 Jy until approximately 2005 (Lister et al. 2019). Since the middle of 2006 however, 0723-008 has become a highly variable radio source with multiple flares. From September 2011 on, the measured flux density has continuously exceeded 3.8 Jy reaching up to 7.6 Jy. This blazar is the brightest source in the radio regime within the MIC sample and has a spectroscopic redshift of $z = 0.127$. As seen with 0506+056 as well, the neutrino event

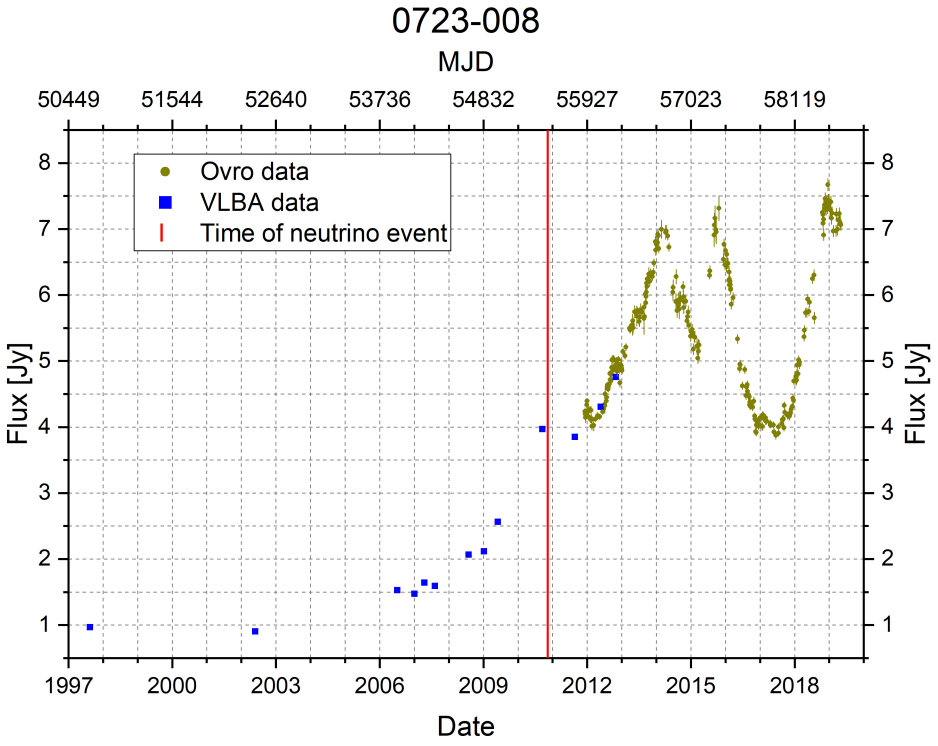

Figure 9: Total flux density of the BL Lac object 0723-008 at 15 GHz. The VLBA observed this blazar from 1997 until the end of 2012. The OVRO started its observation at the end of 2011.
source: Lister et al. 2019 and the OVRO telescope (OVRO Team, S. Kiehlmann, priv. comm.)

ID 5 seems to occur in a six year long period, in which the flux density of 0723-008 was rising almost continuously from ≈ 1.5 Jy to almost 7.0 Jy.
The image of 0723-008 (Fig. 10) is made from the epoch, that is closest to the neutrino event. The blazar is dominated by its core and does not show any features outside of it that could form a jet. Only in the two earliest epochs (18.08.1997 and 29.05.2002, images at MOJAVE website[9]) a jet can be found, that is extending to the NW. In these two epochs the core had a relatively low flux density, so it is possible that the absence of a jet in later epochs is because it has become to faint in comparison. The major axis of the elliptically fitted core component still displays the same orientation. In almost all epochs, the 15 GHz maps show an increased noise along the NS axis, which indicates that the imaging process was not completely successful. This is likely due to errors in the initial calibration. However, the image can still be used to study the object's morphology. It does not show any properties that are unique in this source, that could support theories concerning a neutrino emission.
None of the observed criteria (Sect. 5.2) are striking in 0723-008. The only properties that could raise attention are the highly variable core dominance (between 0.57 and 0.90 in different epochs), the projected jet length with only 13.5 pc and the projected distance of the components to the core (smaller than 3 pc). In Fig. 10 the source looks very compact, but $\frac{S_{unres}}{S_{VLBA}} \approx 0.5$ hardly confirms that. This is due to one bright component (component 6, Lister et al. 2019) lying very close to the core. It is likely that parts of the core have been interpreted and imaged as a jet feature, explaining the low compactness and the small jet length. Also, this source has a relatively bright halo around its core, that decreases the compactness quite substantially. The

[9]http://www.physics.purdue.edu/astro/MOJAVE/

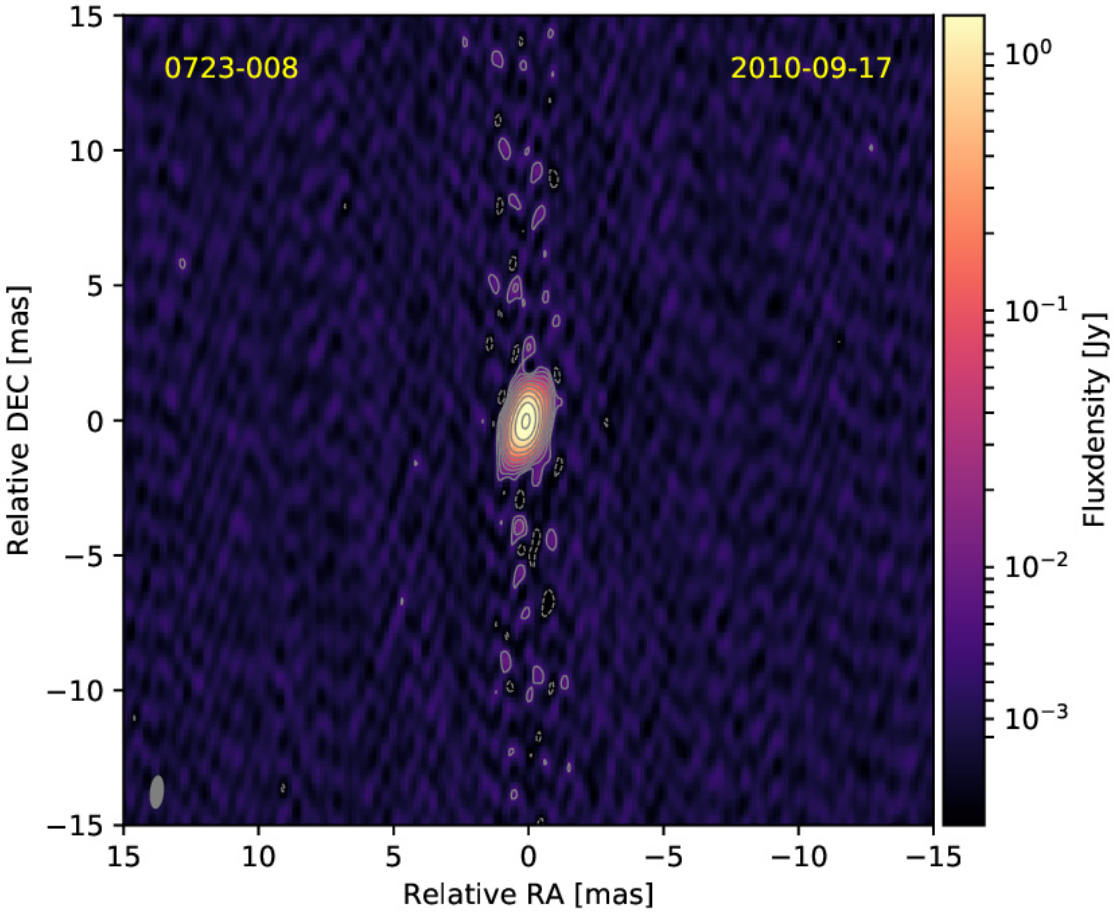

Figure 10: This 15 GHz map of 0723-008 was made with Difmap and data from the MOJAVE website. The lowest contour line is at a level of $3 \times rms$. The epoch seen here is the one that lies closest to the neutrino event (2 months). No components except for the elliptical radio core itself can be found. There are many small noise features that all lie on the NS axis which indicate that an error occurred in the imaging process.

compactness on arcsecond-scales is ≈ 0.9.
0723-008 is relatively bright when compared to the MOJAVE sample. With a flux density of 2064 mJy it is included in the top 15% brightest of all sources.
However, this source is rather ordinary, especially when analysing regarding the criteria kinematics and polarisation. $|P.A. - V.A.|$ does not exceed 30 degrees and the fastest component exhibits a β_{app} of only 1.04. The core polarisation has a median of 1.1% and a maximum of 1.7% which is common among the MOJAVE sample.

5.3.3 1038+064

The radio blazar 1038+064 is identified as a FSRQ (Lister et al. 2019) and has already been a part of the Original MOJAVE sample introduced by Lister et al. (2009). In Garrappa et al. 2019, this source is identified as a possible counterpart to the neutrino event IC-141209A. Their paper focuses on two blazars, GB6 J1040+0617 and 1038+064, that are in spatial coincidence to the neutrino detection. As the source 1038+064 is included in the MOJAVE program, it will be examined further here[10]. The spatial difference between the neutrino event and the blazar is 0.458 degrees (27.5 arcminutes), which is well within the 90%-containment area.
The OVRO light curve does not reveal any major developments in the time between 2008 and 2019. The flux density varies between 0.8 Jy and 1.6 Jy with several flares and minima. Data

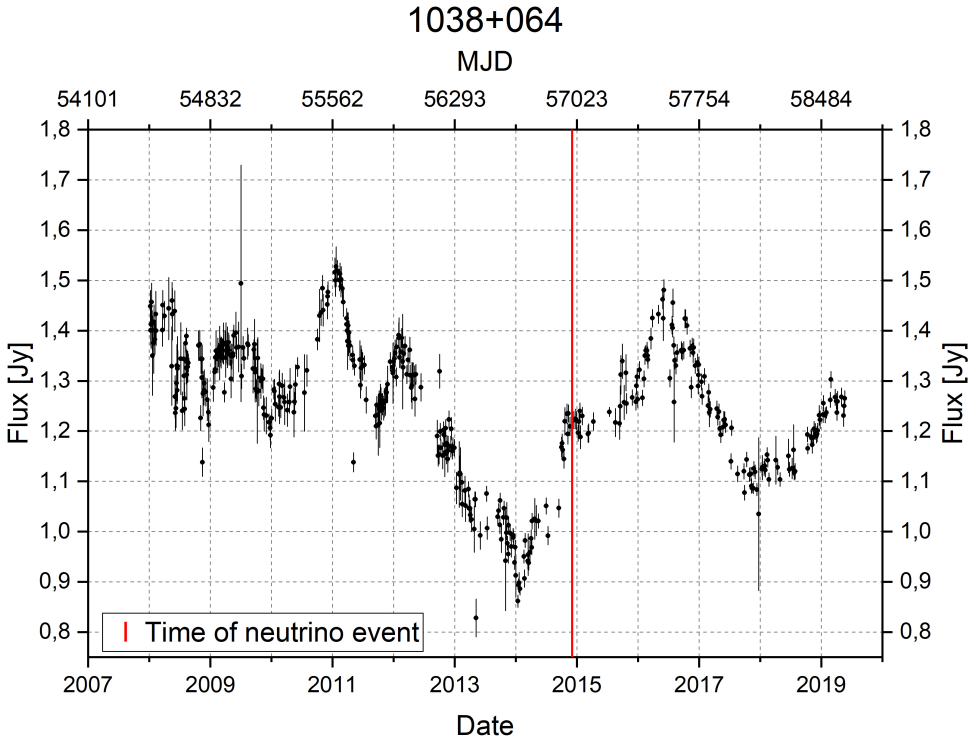

Figure 11: Total flux density of the FSRQ object 1038+064 from 2008 until 2019. This measurement was made by the OVRO telescope at a frequency of 15 GHz.
source: OVRO telescope website: http://www.astro.caltech.edu/ovroblazars/

from MOJAVE (Lister et al. 2019) shows that the flux density has primarily been decreasing since 1998. This tendency can also be found in the OVRO data (see Fig. 11). The light curve shows a minimum in the beginning of 2014 at only 0.84 Jy. No unusual developments can be seen in the lightcurve around the time of the neutrino event.
The image of 1038+064 (Fig. 12) represents a rather typical MOJAVE blazar. A jet consisting of three components is extending to the SE. The first feature, the biggest one, lies close to the core. A faint, second one, seems to extend south from this first feature. The last component has a similar position angle as the first one but is located further away from the core with a $d = 61,6$pc.

[10]GB6 J1040+0617 is faint in the radio band with a flux density $F_{1.4\text{GHz}}$ and $F_{5\text{GHz}}$ below 50 mJy (Maselli et al. 2015)

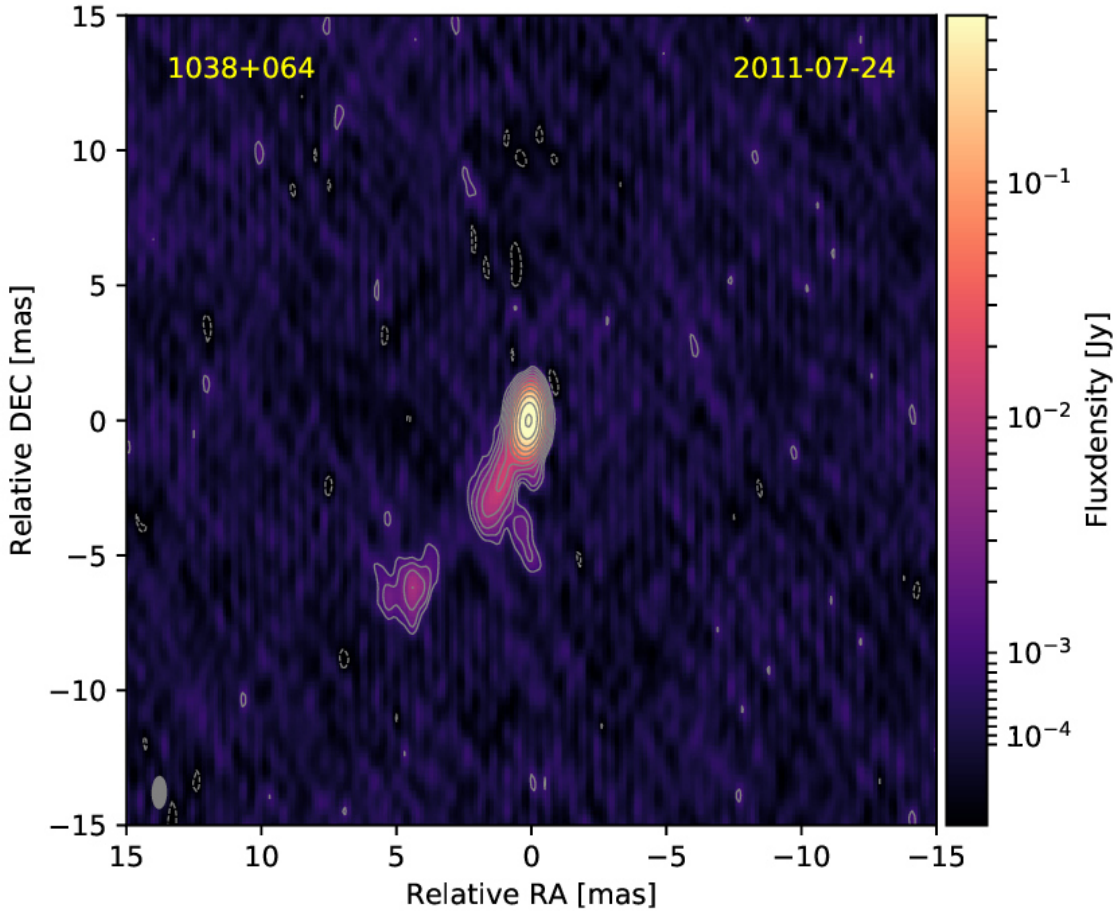

Figure 12: This 15 GHz map of 1038+064 was made with Difmap and data from the MOJAVE website. The lowest contour line is at a level of 3 × rms. The epoch seen here is the one that lies closest to the neutrino event (40 months). The background noise seems evenly distributed. One can see a jet consisting of two major features extending away from the core towards the SE.

In the epochs until 2005, both, the compactness on mas-scales and the core dominance, were varying in between 0.5 and 0.85. Approximately half of all MOJAVE blazars have similar values for $\frac{S_{unres}}{S_{VLBA}}$ and $\frac{S_{core}}{S_{VLBA}}$. The compactness on arcsecond-scales, however, is relatively high, and even exceeding the value 1 (Kovalev et al. 2005). This is not unique among the MOJAVE sample, but it is obvious that this source appears as a point source in kpc-scales. Similar to 0723-008, this blazar also has one very bright component (component 5, $S_{15\mathrm{GHz}} = 272$ mJy, Lister et al. 2019) lying close to the core.

Generally, this source seems to represent the standard model of a blazar fairly well (Pushkarev et al. 2017, Lister et al. 2019). The jet is highly collimated with an apparent opening angle of 11.2 degrees and a parabolic shape. The blobs move radially outwards with apparent superlumnial jet speeds (β_{app} between 3 and 10). The jet is relatively long. Most jet features seem to be located further from the core than average, so the projected jet length is $\approx$ 70 pc. There is also a faint component with a $d \approx 60$ pc. Only 5.1% of all features lie this far out from the core. However, with 14 identified components in the MIC sample, it is not surprising to find an outlier like this. The polarisation of the core of 1038+064 does not vary from the average polarisation of the MOJAVE sample.

5.3.4 1502+106

The IceCube high-energy neutrino IC-190730A was located 0.3098 degrees (18.6 arcminuntes) from 1502+106 within the 90% containment area (Taboada Stein 2019, ATel 12967). Therefore, several publications, for example Kiehlmann et al. (2019, Atel 12996), argue that 1502+106 is a candidate neutrino source.
This theory is supported by the current developments in the OVRO light curve. Until 2014 the

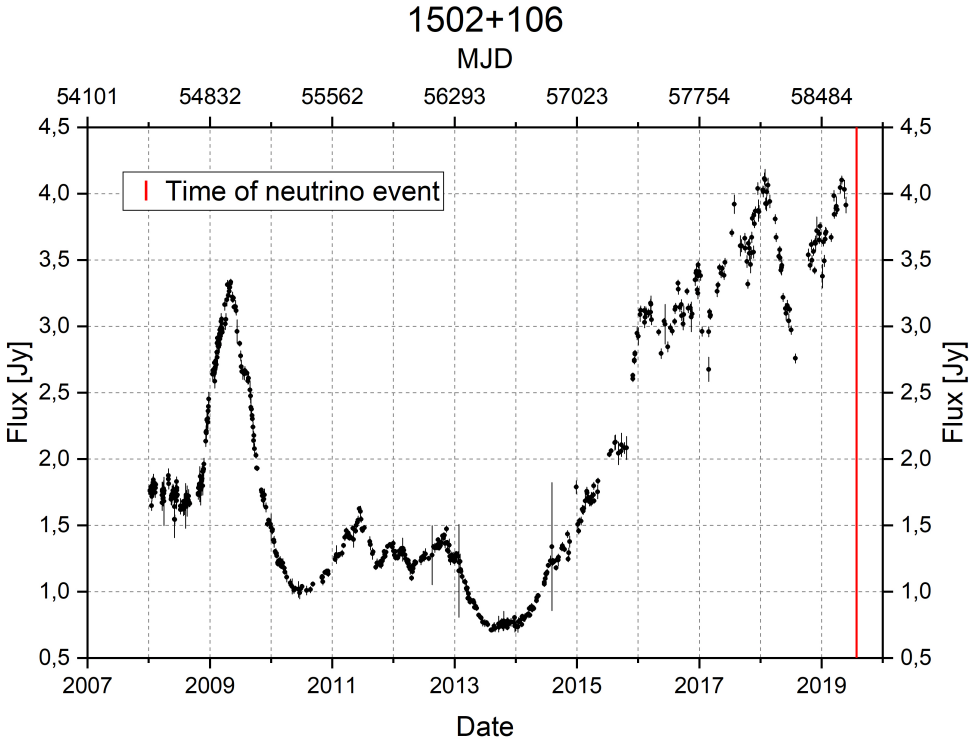

Figure 13: Total flux density of the FSRQ object 1502+106 over a time span of 11 years. This measurement was made by the OVRO telescope at a frequency of 15GHz.
source: OVRO telescope website: http://www.astro.caltech.edu/ovroblazars/

flux density is relatively stable between 1 Jy and 2 Jy, even though there are some flares, e.g. in 2009. Since 2014 there has been a clear tendency of rising flux density that currently exhibits a maximum. It should be noted, that this AGN is very bright. Its median flux density is above average with 1.2 Jy even though its redshift $z = 1.838$ clearly surpasses the median redshift of the MOJAVE sample $z_{MOJAVE} = 0.87$ (Lister et al. 2019). 1502+106 has been a part of the Original MOJAVE sample (Lister et al. 2009) and was first observed in 1997. It is also included in the *Fermi*-MOJAVE sample due to an integrated *Fermi*-LAT energy flux density > 0.1 GeV.

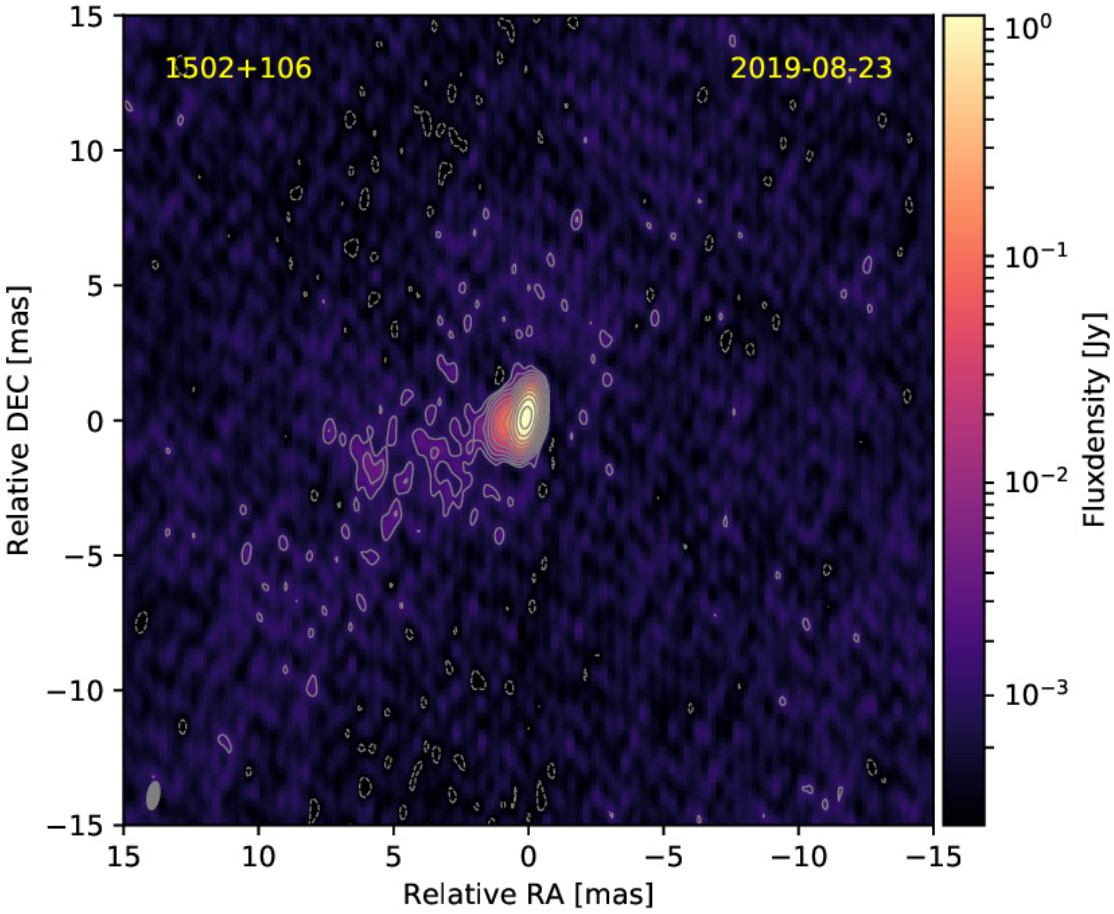

Figure 14: This 15 GHz map of 1502+106 was made with Difmap and data from the MOJAVE website. The lowest contour line is at a level of 3 × *rms*. The epoch seen here is the one that lies closest to the neutrino event (3 weeks). The noise is not completely random but concentrated around the middle of the map. However, the image can still be seen as a valid representation of the blazar. A jet component and some low luminosity features can be found to the east of the core.

The observational data used for Fig. 14 was gathered on 23.08.2019. It is the epoch lying closest to the neutrino event. Here, a jet can be found that is extending to the east from the core. The major axis of the elliptically fitted core component is not aligned with the jet axis, but almost perpendicular to it (approximately 80 degrees). This is a rare feature and only occurs in ≈ 10% of all MOJAVE sources (Kovalev et al. 2005). However, this offset may be created by the shape of the beam in this image (see bottom left corner in Fig. 14). It is closer to ≈ 50 degrees in most other epochs. The compactness on mas-scales, the core dominance, and the polarisation of the core seem to represent a typical MOJAVE blazar.

Cooper et al. (2007) present the kpc morphology of this source (see Fig. 15). The core of 1502+106 is rather dominant in this image, and as a result the compactness on arcsecond-scales is close to 1. This value is very common, and appears in almost every third of the MOJAVE sample. In Fig. 15, the AGN shows a jet, that almost perfectly aligns with the core component's major axis seen in the mas-scale image (Fig. 14).

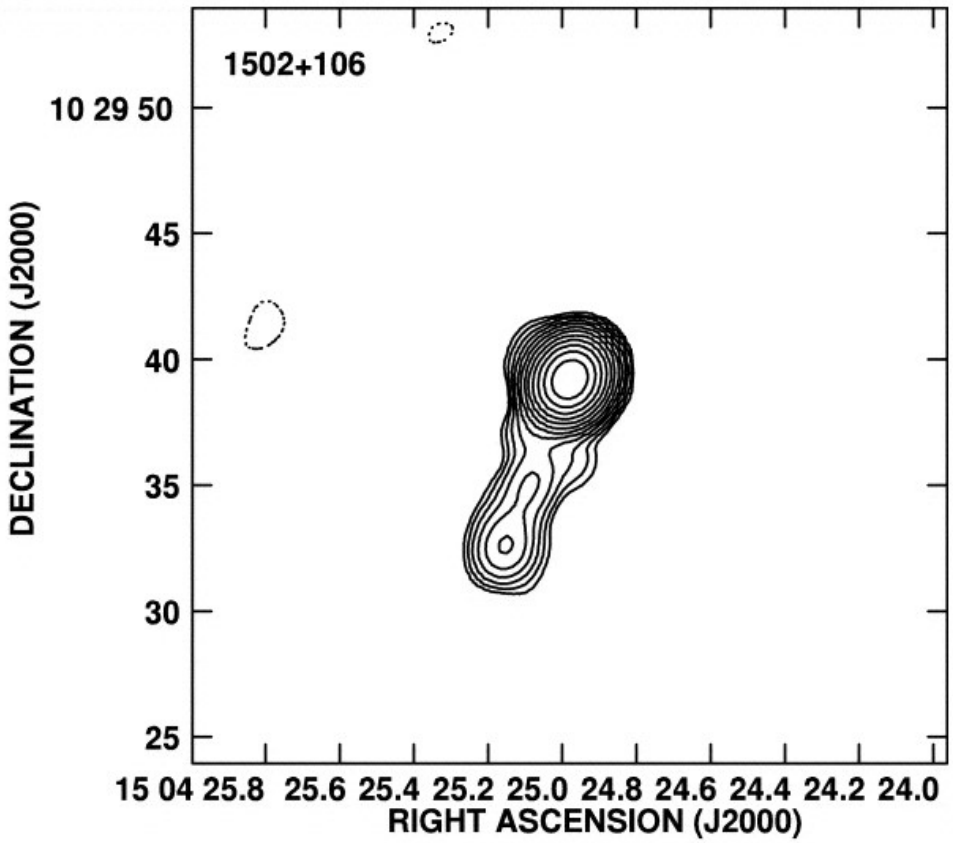

Figure 15: 1.4 GHz image of 1502+106 from the VLA in A configuration. The image was created using Difmap and shows the source's kpc morphology.
source: Cooper et al. 2007

The jet, however, shows a few remarkable features. Most blobs move along the jet with highly relativistic speeds up to $\beta_{app} = 18.2$. Also, of the slower features, one moves almost perpendicular to the jet axis, with $|P.A. - V.A.| = 70°$. Furthermore, the four components from Lister et al. (2019, Table 3) are relatively bright ($S_{15GHz} \in [100\text{Jy}, 200\text{Jy}]$) when compared to other jet features in the MOJAVE sample, and the jet length $L = 55,4$ is also slightly above average. The shape of the jet is almost conical due to a k-index of 1.02, and the apparent jet opening angle is a clear outlier with 37.6 degrees. Only approximately 12% of all sources show an α_{app} over 37 degrees.
None of these attributes is highly unlikely, however, it is remarkable they all appear in one source. Therefore, when observing its radio properties, 1502+106 seems to be the AGN in the MIC sample that has the least resemblance with an average MOJAVE blazar.

5.4 Sample analysis

None of the four analysed sources (see Sect. 5.1) displayed any unique properties on its own, so that the blazar could be labelled as special or unconventional due to its radio emission. This chapter is supposed to find, whether there are unique properties that all sources from the MIC sample share.
For once, three of the MIC sources, all except 1038+064, display a major rise in flux density in the years around the time of the neutrino event.
The IC-170922A event took place approximately in the middle of the three years, where 0506+056 tripled its flux density from about 0.5 Jy to 1.5 Jy. 0723-008 shows a similar behaviour. The flux density of this source has been rising from 1.5 Jy in 2008 to almost 7.0 Jy in 2014, with the possible neutrino emission in the end of 2010.
It is too early to draw a similar conclusion for 1502+106. However, this blazar has shown a major outburst that started in 2014 and lasted at least until the time of IC-190730A.
There is another blazar close to 1038+064, GB6 J1040+0617, that may also be responsible for IC-141209A (Garrappa et al. 2019). Since the energy of this neutrino is ≈ 100 TeV, it would also be reasonable to assume, that this neutrino was produced in a scattering process in the atmosphere. This could lead to the conclusion, that 1038+064 should not be included in the MIC sample. The other three blazars all exhibit a major increase of brightness around the time of their possible associated neutrino event, which probably is the best link between these MIC blazars and a possible neutrino production. However, due to the fact that most blazars show high flux variability, this may also just be a coincidence.
In order to find other attributes that stick out, the MIC sample is compared to the MOVAJE sample regarding some selected numerical values (see Sect. 5.2). Since MOJAVE contains over 300 observed AGN, this collection is a fair representation of all observable blazars. The comparison is done by analysing the distributions of one numerical feature in both samples.
To demonstrate these distributions, they are plotted in histograms, one for each of the mentioned criteria. In addition, a statistical test, a Kolmogorov Smirnov Test (KS test), was performed. This test examines how likely two samples of data were taken from the same overall distribution. The KS test is the quasi standard when comparing samples in astrophysics, even though its validity has limitations in case of small sample sizes. It compares two relative distribution functions regarding a single random variable. It provides a p-value, that states the likelihood of the differences in the two distributions to simply occurred by chance.
$p = 1$ states, that the distributions are identical. The smaller p gets, the higher is the likelihood, that these two compared samples differ. However, the interpretation of the KS-Test depends on the context.
In this case, the p-value indicates how likely it is that the MIC sources and their numerical properties were chosen at random, given that the MOJAVE sample is a fair representation of all blazars. Since the MIC sources are so few, an identical distribution is not only highly unlikely but, in most cases, also impossible. Also, one outlier in one of the four sources can heavily influence the outcome of the KS-Test.
Here a value of p in between 1 and ≈ 0.3 can easily be interpreted as the two samples not exhibiting any major differences. If p is lower than ≈ 0.3, it is possible that the two samples differ regarding the tested variable. However, a p this low would be expected in almost every third sample, consisting of four randomly selected MOJAVE blazars. Only a p smaller than ≈ 0.05 would indicate strongly, that there is a notable difference between MIC and MOJAVE sample. All p-values are listed in Table 5, along with the criterion that was analysed in the related KS-Test.

Criterion	p-value
F_{15GHz}	0.3823
S_{15GHz}	0.7478
$\frac{S_{VLBA}}{S_{tot}}$	0.1145
$\frac{S_{unres}}{S_{VLBA}}$	0.1466
$\frac{S_{core}}{S_{VLBA}}$	0.6701
β_{app}	0.8200
$\lvert P.A. - V.A. \rvert$	0.9064
d	0.5893
L	0.9627
α_{app}	0.7563
k	0.5387
m_{med}	0.2508
m_{max}	0.1740

Table 5: The MOJAVE and MIC sample were compared regarding several criteria with a KS-Test. The p-values resulting from this test indicate, how similar the two distributions are.

The KS test is not ideal for this problem. The small sample-size of MIC could create problems because a single outlier can already distort the whole MIC sample's distribution and influence the p-value relatively strong. However, this statistical test is still sensitive to major differences in the two samples. Also, the KS-test is independent from any binning.
In the histograms, the portrayed values are binned, influencing this form of representation to some degree. Still, these graphs help with a qualitative comparison between MOJAVE and MIC samples.

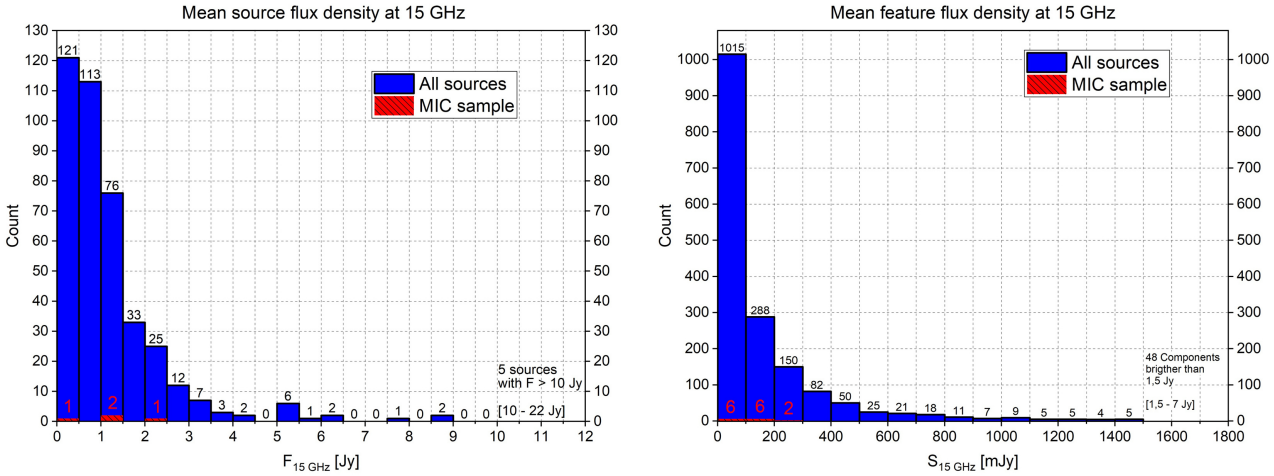

Figure 16: These histograms depict the brightness of the observed MOJAVE sources (Lister et al. 2019). The graph on the left shows how many observed AGN are how bright. Approximately $\frac{3}{4}$ of all sources have a flux density under 1.5 Jy, only very few exceed 4 Jy. On the right side, the brightness of every identified component in the MOJAVE sample is shown in the histogram. The majority of features are less luminous than 100 mJy, however, some are even brighter than 1 Jy. In both graphs the sources/features with the highest flux density have been excluded due to their low quantity and to improve visuals.

In neither of the two flux-density-related histograms, the distribution of MIC and MOJAVE sample seem to fit each other. This, however, is not very surprising, considering that the MIC sample, and the number of features it contains, is quite small. According to the KS test, the probability of four sources, that were selected at random, to yield similar values for $F_{15\mathrm{GHz}}$ and $S_{15\mathrm{GHz}}$ is not very uncommon. This implies that the flux density distribution of the blazars, and their components, is not unique in the MIC sample.

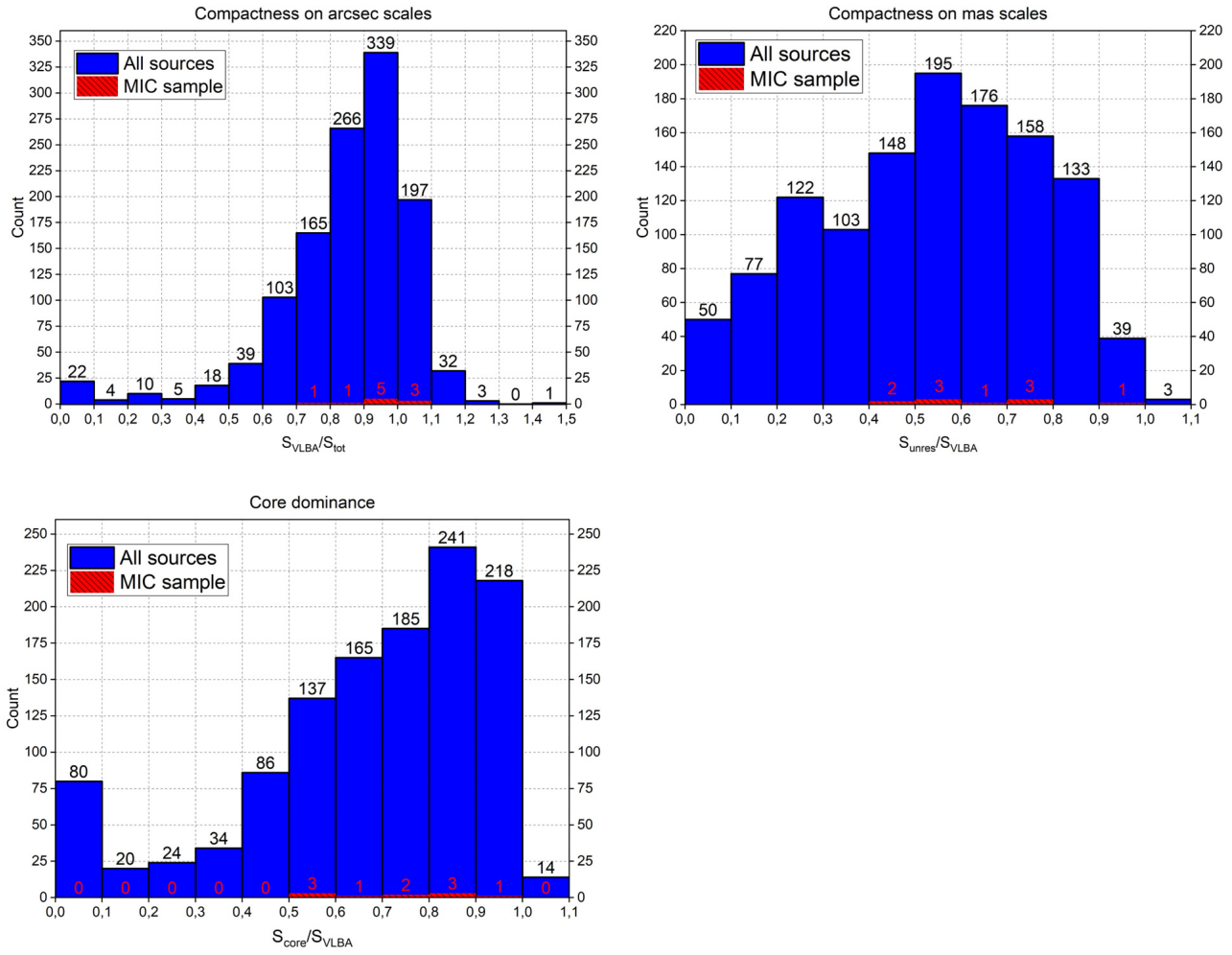

Figure 17: Compactness states, how well the model of a point source would fit the measured brightness distribution. It is a property of the AGN that can be categorised in compactness on arcsecond-scales, compactness on mas-scales, and core dominance. A low value indicates many extended features, while a compactness of 1 would mean that the source is point-shaped in the pane of the sky.

The compactness on all scales (arcsecond, mas, core dominance) also does not reveal any special attributes of the MIC sample. The p-values of the KS tests are rather small, with the compactness on arcsecond-scales having the smallest p in all analysed criteria. However, they are all still above 0.1. These small values seem logical, because the MOVAJE distributions are quite broad. Also, from the plots it seems, as if the distributions align with the MOJAVE sources fairly well.
Contrary to most other histograms, these plots exhibit less of a clear maximum. Especially the compactness on mas-scales and the core dominance stretch from 0.4 to almost 1.0. There is a tendency in all three histograms of rising compactness, up until somewhere between 0.6 and 0.9, that ends in a steep flank, at approximately 1.

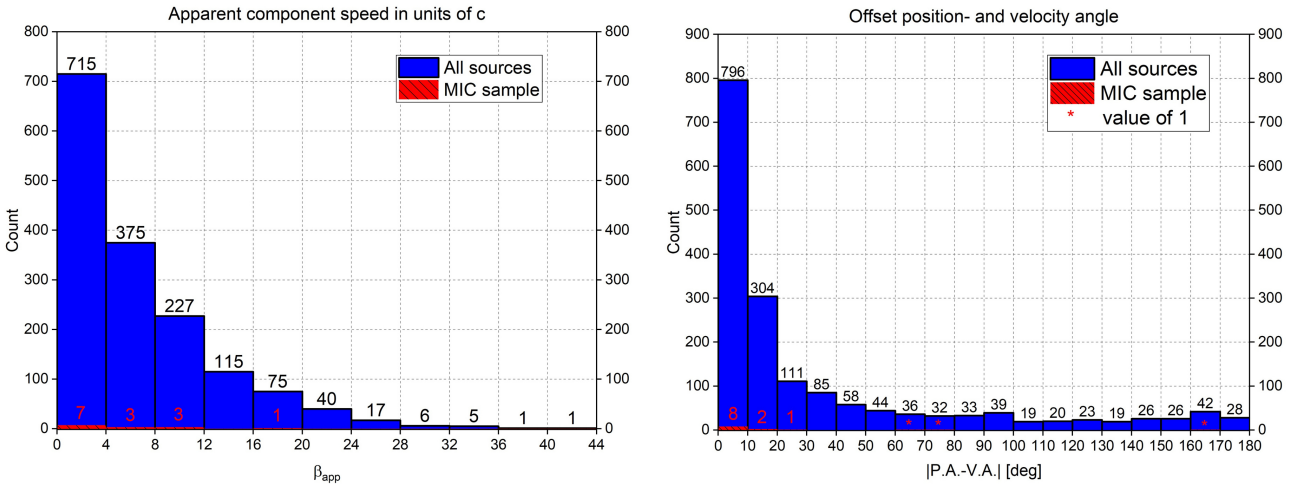

Figure 18: Both graphs show properties of all features in the MOJAVE sample. The distribution of apparent jet speed (left) shows that almost half of all features have a $\beta_{app} \leq 4$. The Distribution of $|P.A. - V.A.|$ (right) shows clearly that about $\frac{2}{3}$ of all features are aligned in a jet. However, there is some kind of ground level with an amplitude of ≈ 30 sources per 10 degrees that do not seem to move along the jet axis. The MIC and MOJAVE components seem to be distributed almost identical

When observing the kinematic properties, the two samples do not show any obvious signs for differences. The observed criteria are measured for every jet feature, so both samples have a relatively large size. This benefits the validity of the KS-test, that states, that for both properties the distributions match very well.
The histogram of β_{app} shows a development similar to an exponential decay. Almost half of all components do not exceed an apparent velocity of $4c$. However, there are only very few (≈ 100) components with $\beta_{app} \leq 1$. This means that in most jets the blobs move along the jet with a high relativistic speed and the projection effect (see Sect. 3.2) takes place. The fastest measured components even have $\beta_{app} \geq 30$. The histogram of the offset between position and velocity angle shows that most jets are very collimated. Even though the projection effect makes the jet opening angle appear much wider, a clear majority of sources seems to follow the direction in which the jet is extending. Still, the movement of about a third of all blobs is not ballistic. These features do not move solely outward but follow a curved trajectory. This shows that there must be some kind of acceleration processes in the jet. Lister et al. (2019) even present a complete Table of jet components that have been subject to acceleration.

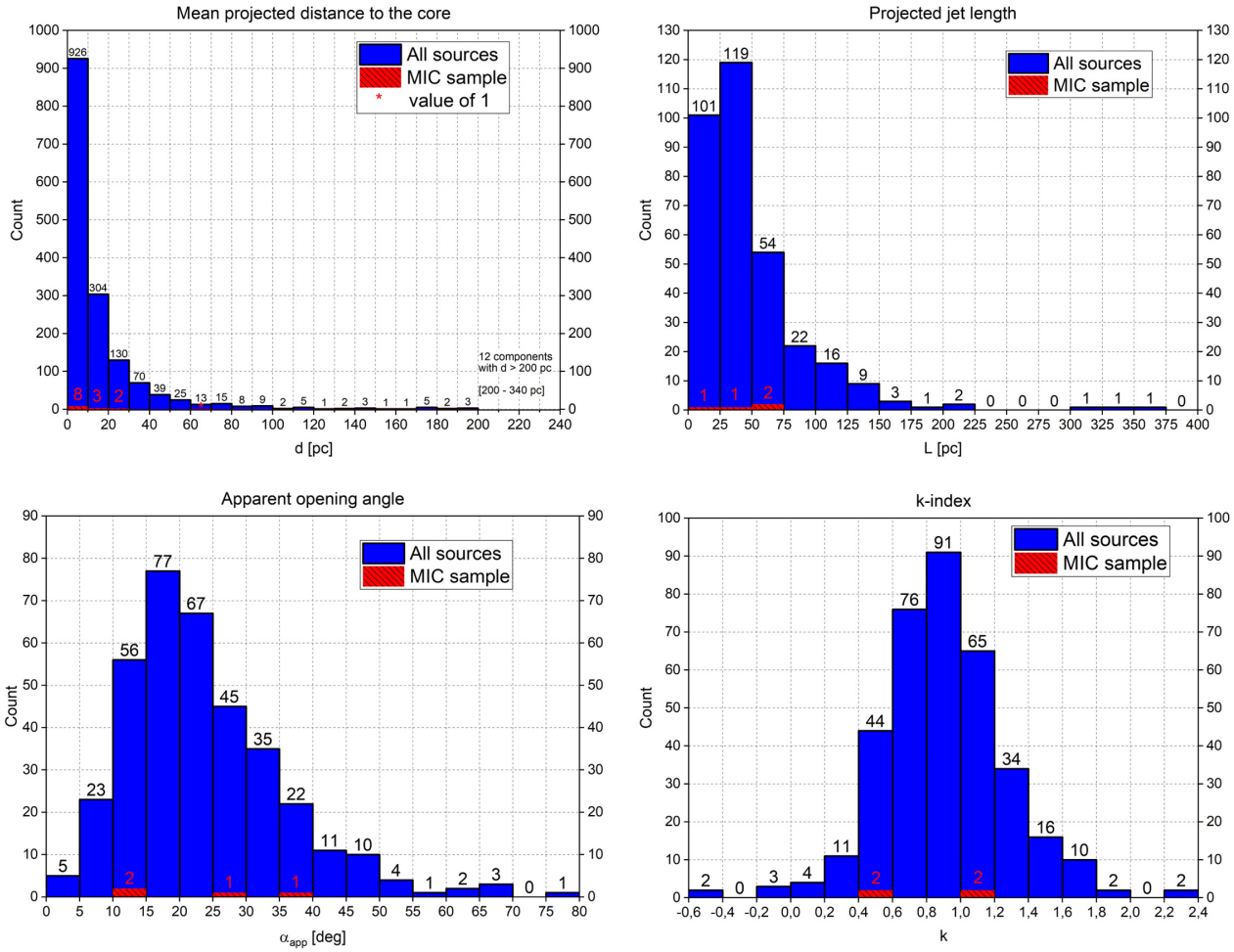

Figure 19: The properties in these graphs describe the form of a jet. The values are not solely intrinsic values of the AGN because of the projection effect. The top left histogram gives the distance of all components to their radio core. This value is computed for one component by calculating the mean core distance over all its epochs. The majority of all features is located relatively close to the core. A similar distribution can be seen in the projected jet length (top right). This distance L is a property of the AGN that is computed by using only the jet feature furthest from the core. The distribution of the apparent opening angle of the jet (bottom left) has a prominent maximum between 10 and 25 degrees. The k-index describes the relation between jet diameter and the core distance. Its distribution (bottom right) has a maximum between 0.6 and 1.2, which means that most jets are shaped conically with a slight tendency to a parabolic shape.

The distributions of a features mean projected core distance in the two samples only show minor differences. But even though the attributes d and L are closely related, this similarity cannot be seen in the projected jet length. Still, the KS test indicates that four sources from the MOJAVE sample, chosen at random, are highly likely to have similar jet lengths. In this case, the binning in the histogram could be responsible for the deviation between the distributions. Due to the small sample size it is not obvious if the distributions of k-index and apparent opening angle in the MIC sample align with the MOJAVE sample. The KS test however reveals that the MIC values of k and α_{app} are common among MOJAVE blazars.

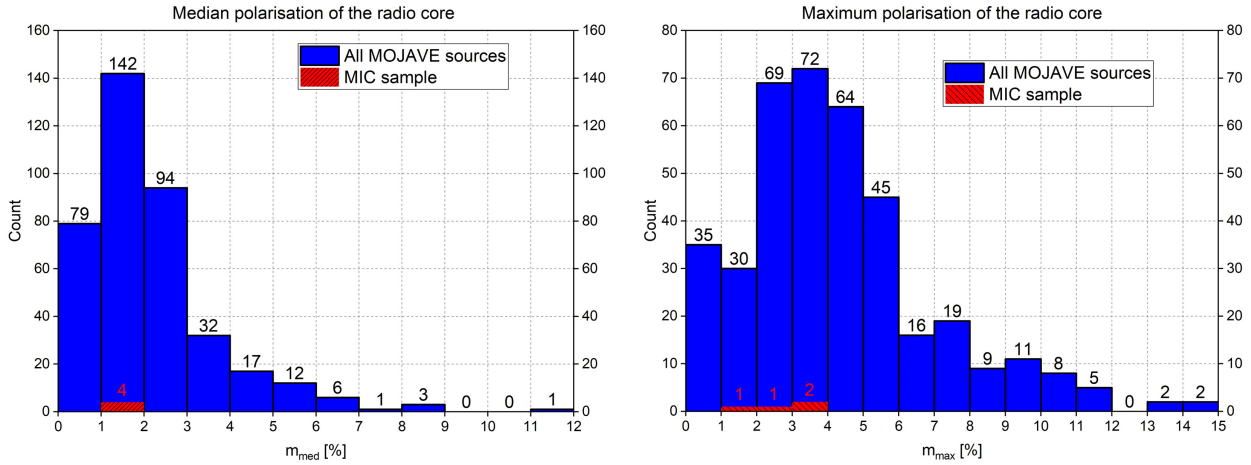

Figure 20: The polarisation of the radio core was computed for every epoch in all sources. The values presented in the distribution (left) are the medians of all epochs. The right graph presents the maximum polarisation the sources had at any epoch. For both quantities the MOJAVE distribution has a relatively broad peak. All MIC sources are located near these maxima.

Finally, the core polarisation of the two samples are compared. Here the p-values are rather small. Again, this is probably due to the broad distributions of the MOJAVE sources. In the histograms there is no major difference between MIC and MOJAVE sample. For m_{med} all MIC values are actually located at the maximum of the MOJAVE distribution. It should be noted, that in this case the KS-Test is flawed as well, because of the small quantity of MIC sources.

6 Summary

Neutrinos are elementary particles that are very hard to trace, because they only interact with gravity and the weak nuclear force. Anyhow, there are telescopes searching for astrophysical neutrinos. In 2018, IceCube claimed that the blazar TXS 0506+056 is a neutrino source with a 3σ confidence level (IceCube Coll. 2018). This association would make it the third known astrophysical object to emit neutrinos. Therefore, this discovery launched the search for other AGN, that could also be a possible neutrino event counterpart.
The energy of a neutrino is a good indicator, to where it originated from (Katz & Spiering 2012). It is very likely, that neutrinos with energies over a hundred Tev are produced by astrophysical sources. However, neutrinos with only a few dozen TeV, like e.g. ID 5 and ID 63, could also be produced by scattering processes in the atmosphere. This means, that some blazars, that are in spatial coincidence with a neutrino event but are actually not the source of any measured neutrino, should be excluded when analysing high-energy neutrino emitting blazars. It is however possible, that some of these sources are included in the MIC sample.
Four blazars, that are candidates for neutrino emission, and are included in the MOJAVE program, have been analysed regarding their radio VLBI properties (the MIC sample from Sect. 5.1). 15 GHz maps were created and the sources OVRO light curves were plotted. None of these figures showed any unique features. Also, several characteristic properties in a blazar were collected for these four sources, and then compared to the average MOJAVE source. Kolmogorov Smirnov tests showed, that the MIC sample and the MOJAVE sample do not differ strongly in any of the analysed criteria from Sect. 5.2.
In conclusion, there is no obvious parameter in the radio spectrum of the MIC sources that would clearly distinguish them from most other blazars. None of the AGN sticks out regarding one of the analysed criteria. The 15 GHz images, the OVRO light curves, and the numeric properties all did not provide evidence of any unusual behaviour in these sources.
The MIC sample itself does not differ radically from any other collection of four MOJAVE blazars, chosen at random. The only notable characteristic, seen in three of the four MIC sources, is the development of the flux density around the time of the high-energy neutrino event. In 0506+056, 0723-008 and 1502+106 the neutrino was detected within a period, stretching over approximately four years, in which the sources brightness increased strongly. However, flares appear relatively often in blazars, so this could be a coincidence.
From the histograms it appears as if the MIC sources, or their components, are rather average when compared to the MOJAVE sample. The p-values from the KS tests were mostly larger than 0.3 and always exceeded 0.1. Only a p-value smaller than 0.05 would have indicated unique properties of the sample.
This does not imply that these sources cannot be special in other wavelength bands. Also, it could be possible that an analysis, correlating the given criteria, might find abnormalities in the MIC sample.
Generally, the statement of this thesis could easily be improved, if more blazars, associated with a neutrino event, were included in the MIC sample. The fact, that only so few high-energy neutrinos have been found, and even fewer are associated with an AGN, limits the ability to draw statistical conclusions. Additionally, these few neutrino associations are not yet reliable enough to find a clear context between them, and a possible counterpart in the electromagnetic spectrum.
All of these problems can be solved by further neutrino observations. Currently IceCube detects

one neutrino with an energy over 10^{13} eV in approximately 25 days[11]. With the planned second generation of IceCube, the IceCube-Gen2[12], this time span is expected to decrease substantially. Therefore, it is only a matter of time until more neutrinos are found, that are in spatial coincidence with blazars. A higher number of neutrino events could possibly make it a lot easier to confirm, that one of these particles originates from a single known source.
Finally, a broadband analysis of all known neutrino-emitting blazar candidates may already be able to find a connection between those sources. Especially the γ-regime should be analysed further in possible AGN counterparts. This is due to the known link between the production of high-energy photons and high-energy neutrinos (Tavecchio et al. 2014).

[11]Interpolation with the neutrino events from Aartsen et al. 2014 and IceCube Coll. 2017
[12]https://icecube.wisc.edu/

Acknowledgements

I would like to thank all members of the Chair of Astronomy of the University Würzburg for creating a productive and colloquial environment. In my time at the department I have felt welcome and supported.

Special thanks go to my supervisor Prof. Dr. Matthias Kadler. First of all, he offered me to do my Bachelor thesis in Astronomy. Also, he was giving the lecture that introduced me to astrophysics in the first place. Mostly, he helped with any problem I had, whether it was regarding scientific context or any other issue with my work.
I would also like to thank Prof. Dr. Karl Mannheim for accepting me as a Bachelor student at the Chair of Astronomy.

Also, I would like to thank Paul Ray Burd for introducing me to radio astronomy. His help started with a course into Difmap and extended to many software related problems, that occurred during the time when I was working on my Bachelor's degree.
Marcus Langejahn and Luis Wachter have also been supporting me, especially with technical issues, whenever I was asking for their help.
Finally, I would also like to thank my parents for the support I have been receiving throughout the whole time of my studies as well as for the help improving my English writing skills.

This research has made use of data from the MOJAVE database that is maintained by the MOJAVE team (Lister et al., 2018, ApJS, 232, 12).

This research has made use of data from the OVRO 40-m monitoring program (Richards, J. L. et al. 2011, ApJS, 194, 29) which is supported in part by NASA grants NNX08AW31G, NNX11A043G, and NNX14AQ89G and NSF grants AST-0808050 and AST-1109911.

This research has made use of ISIS functions (ISISscripts) provided by ECAP/Remeis observatory and MIT (http://www.sternwarte.uni-erlangen.de/isis/).

Partly based on observations with the 100-m telescope of the MPIfR (Max-Planck-Institut für Radioastronomie) at Effelsberg.

Declaration of authorship

All requirements of the ASPO §26 were met when writing this thesis. It was written only by the declared author Philip Weber. All papers that are cited and sources used are listed, either directly in the thesis or in the section "References". The thesis has not been released to any other institution previous to the stated release date (nor will it be published simultaneously).

Beim schreiben dieser Arbeit wurden alle Vorgaben der ASPO §26 wurden eingehalten. Sie wurde ausschließlich vom erklärten Autor Philip Weber verfasst. Alle zitierten Artikel und verwendeten Quellen sind ordnungsgemäß aufgeführt, entweder direkt in der Arbeit oder in "References". Diese Arbeit wurde nicht vor dem angegebenen Abgabedatum (und wird auch nicht gleichzeitig) einer anderen Prüfungsbehörde vorgelegt.

Place, Date	Signature
Ort, Datum	Unterschrift

References

Aartsen, M. G., et al. 2014, "Observation of High-Energy Astrophysical Neutrinos in Three Years of IceCube Data", Phys. Rev. Lett., 113, 101101

Abdo, A. A., et al. 2009, "The on-orbit calibration of the Fermi Large Area Telescope", Astropart. Phys., 32, 193

Abdo, A. A., et al. 2011, "Fermi Large Area Telescope Observations of Markarian 421: The Missing Piece of its Spectral Energy Distribution", ApJ, 736, 131

Beckmann, V., Shrader, C. R. 2012, "Active Galactic Nuclei", Wiley-VCH, Berlin

Britzen, S., et al. 2019, "A cosmic collider: Was the IceCube neutrino generated in a precessing jet-jet interaction in TXS 0506+056?", A&A, 630, A103

Cooper, N. J., et al. 2007, "MOJAVE: Monitoring of Jets in Active Galactic Nuclei with VLBA Experiments. III. Deep VLA Images at 1.4 GHz", ApJS, 171, 376

Fanaroff, B. L., Riley, J. M. 1974, "The morphology of extragalactic radio sources of high and low luminosity", MNRAS, 167, 31P

Fukuda, S., et al. 2003, "The Super-Kamiokande detector", Nucl. Instrum. Meth., 501, 418

Garrappa, S., et al. 2019, "Investigation of Two Fermi-LAT Gamma-Ray Blazars Coincident with High-energy Neutrinos Detected by IceCube", ApJ, 880, 103

Ghisellini, G., et al. 2005, "Structured jets in TeV BL Lac objects and radiogalaxies. Implications for the observed properties", A&A, 432, 401

Hodge, M. A., et al. 2018, "MOJAVE XVI: Multiepoch Linear Polarization Properties of Parsec-scale AGN Jet Cores", ApJ, 862, 151

Högbom, J. A. 1974, "Aperture Synthesis with a Non-Regular Distribution of Interferometer Baselines", A&AS, 15, 417

Homan, D. C., et al. 2002, "Parsec-Scale Blazar Monitoring: Flux and Polarization Variability", ApJ, 568, 99

IceCube Collaboration et al. 2006, "First year performance of the IceCube neutrino telescope", Astropart. Phys., 26, 155

IceCube Collaboration et al. 2017, "The IceCube Neutrino Observatory - Contributions to ICRC 2017 Part II: Properties of the Atmospheric and Astrophysical Neutrino Flux", arXiv e-prints, 1710.01191

IceCube Collaboration et al. 2018, "Neutrino emission from the direction of the blazar TXS 0506+056 prior to the IceCube-170922A alert", Science, 361, 147

Kassim, N. E., et al. 1993, "Subarcminute Resolution Imaging of Radio Sources at 74 MHz With the Very Large Array", AJ, 106, 2218

Katz, U. F., Spiering, C. 2012, "High-energy neutrino astrophysics: Status and perspectives", Prog. Part. Nucl. Phys., 67, 651

Kellermann, K. I., Moran, J. M. 2001, "The Development of High-Resolution Imaging in Radio Astronomy", ARA&A, 39, 457

Kellermann, K. I., et al. 1989, "VLA Observations of Objects in the Palomar Bright Quasar Survey", AJ, 98, 1195

Kellermann, K. I., et al. 1998, "Sub-Milliarcsecond Imaging of Quasars and Active Galactic Nuclei", AJ, 115, 1295

Kiehlmann, S., et al. 2019, "Neutrino candidate source FSRQ PKS 1502+106 at highest flux density at 15 GHz", ATel 12996

Kovalev, Y. Y., et al. 2005, "Sub-Milliarcsecond Imaging of Quasars and Active Galactic Nuclei. IV. Fine-Scale Structure", AJ, 130, 2473

Kovalev, Y. Y., et al. 2019, "Discovery of geometry transition in nearby AGN jets", arXiv e-prints, 1907.01485

Kun, E., et al. 2017, "A at-spectrum candidate for a tracktype high-energy neutrino emission event, the case of blazar PKS 0723-008", MNRAS, 466, L34

Kun, E., et al. 2019, "Very long baseline interferometry radio structure and radio brightening of the high-energy neutrino emitting blazar TXS 0506+056", MNRAS, 483, L42

Lind, K. R., Blandford, R. D. 1985, "Semidynamical models of radio jets: relativistic beaming and source counts.", ApJ, 295, 358

Lister, M. L., et al. 2009, "MOJAVE: Monitoring of Jets in Active Galactic Nuclei with VLBA Experiments. V. Multi-Epoch VLBA Images", AJ, 137, 3718

Lister, M. L., et al. 2011, "γ-Ray and Parsec-scale Jet Properties of a Complete Sample of Blazars From the MOJAVE Program", ApJ, 742, 27

Lister, M. L., et al. 2013, "MOJAVE. X. Parsec-scale Jet Orientation Variations and Superluminal Motion in Active Galactic Nuclei", AJ, 146, 120

Lister, M. L., et al. 2018, "MOJAVE. XV. VLBA 15 GHz Total Intensity and Polarization Maps of 437 Parsec-scale AGN Jets from 1996 to 2017", ApJS, 234, 12

Lister, M. L., et al. 2019, "MOJAVE. XVII. Jet Kinematics and Parent Population Properties of Relativistically Beamed Radio-loud Blazars" ApJ, 874, 43

Mannheim, K. 1993, "γ rays and neutrinos from a powerful cosmic accelerator", Phys. Rev. D., 48, 2408

Mannheim, K. 1995, "High-energy neutrinos from extragalactic jets", Astropart. Phys., 3, 195

Maselli, A., et al. 2015, "New blazars from the cross-match of recent multi-frequency catalogs", Ap&SS, 357, 141

Nair, S., et al. 2005, "Helical jet in the gravitationally lensed blazar PKS1830-211", MNRAS, 362, 1157

Napier, P. J. 1994, "The Very Long Baseline Array", Very High Angular Resolution Imaging, by Robertson, J. G., William, J. T., Vol. 185, IAU Symposium, 117

Pushkarev, A. B., et al. 2017, "MOJAVE - XIV. Shapes and opening angles of AGN jets", MNRAS, 468, 4992

Quirrenbach, A., et al. 1992, "Statistics of intraday variability in extragalactic radio sources.", A&A, 258, 279

Richards, J. L., et al. 2011, "Blazars in the Fermi Era: The OVRO 40 m Telescope Monitoring Program", ApJS, 194, 29

Ros, E., et al. 2020, "Apparent superluminal core expansion and limb brightening in the candidate neutrino blazar TXS 0506+056", A&A, 633, L1

Rybicki, G. B., Lightman, A. P. 1979, "Radiative processes in astrophysics", Wiley, New York

Salpeter, E. E. 1964, "Accretion of Interstellar Matter by Massive Objects.", ApJ, 140, 796

Seyfert, C. K. 1943, "Nuclear Emission in Spiral Nebulae.", ApJ 97, 28

Shepherd, M. C., et al. 1994, "DIFMAP: an interactive program for synthesis imaging." BAAS, 26, 987

Taboada, I., Stein, R. 2019, "IceCube-190730A an astrophysical neutrino candidate in spatial coincidence with FSRQ PKS 1502+106", ATel 12976

Tavecchio, F., et al. 2004, "Jets from Subparsec to Kiloparsec Scales: A Physical Connection" ApJ, 614, 64

Tavecchio, F., et al. 2014, "Structured Jets in BL Lac Objects: Efficient PeV Neutrino Factories?", ApJ, 793, L18

Türler, M., et al. 1999, "30 years of multi-wavelength observations of 3C 273", A&AS, 134, 89

Urry, C. M., Padovani, P. 1995, "Unified Schemes for Radio-Loud Active Galactic Nuclei", PASP, 107, 803

van Haarlem, M. P., et al. 2013, "LOFAR: The LOw-Frequency ARray", A&A, 556, A2

Wootten, A., Thompson, A. R. 2009, "The Atacama Large Millimeter/Submillimeter Array", IEEE Proceedings, 97, 1463

Zensus, J. A. 1997, "Parsec-Scale Jets in Extragalactic Radio Sources" ARA&A, 35, 607

Appendix

The images Fig. 8, Fig. 10, Fig. 12 and Fig. 14 were created with the software difmap. The numeric values of each component in these images are given in Table A1 to Table A9.

Flux density (Jy)	Radius (mas)	P.A. (degrees)	Flux density (Jy)	Radius (mas)	P.A. (degrees)
3,96E-01	0,00	0,00	5,19E-04	1,66	-154,98
4,05E-03	0,10	0,00	2,44E-04	1,63	-169,38
3,89E-03	0,41	165,96	1,88E-03	0,81	172,88
5,36E-03	0,20	0,00	4,51E-04	1,44	-146,31
6,90E-03	0,60	-180,00	2,32E-04	2,02	-171,47
1,05E-02	0,30	0,00	4,30E-04	1,75	-156,37
1,36E-02	0,70	-180,00	1,22E-03	0,51	11,31
1,25E-02	0,40	0,00	9,13E-04	1,43	-167,91
9,28E-03	0,80	-180,00	9,13E-04	1,43	-167,91
2,11E-03	0,36	146,31	9,56E-04	2,12	-171,87
2,10E-03	0,45	153,44	2,08E-03	1,91	173,99
9,35E-04	0,71	-171,87	5,94E-04	1,06	-138,81
1,01E-02	0,42	135,00	6,88E-04	1,84	-157,62
5,57E-03	0,81	-172,88	1,79E-04	0,28	-45,00
2,97E-03	0,41	-14,04	1,76E-04	1,53	-148,39
9,01E-03	0,36	-123,69	6,55E-04	1,24	-165,96
1,37E-03	0,90	-180,00	1,22E-03	0,63	161,57
4,92E-03	0,50	0,00	3,58E-04	1,61	-150,26
4,97E-03	1,84	-167,47	3,35E-04	1,33	-167,01
2,72E-03	1,14	-142,13	2,45E-03	3,90	-180,00
4,03E-03	0,51	-11,31	7,52E-04	3,75	170,79
4,20E-03	0,91	-173,66	3,08E-04	1,70	-151,93
3,40E-03	1,92	-171,03	9,10E-04	2,21	-174,81
1,26E-03	0,36	123,69	6,37E-04	0,50	-143,13
2,39E-03	1,22	-145,01	2,86E-04	3,77	169,29
3,78E-04	0,32	-108,44	1,42E-04	1,46	-164,06
5,85E-04	0,92	-167,47	1,48E-03	3,48	161,57
1,60E-03	0,50	143,13	2,58E-04	2,11	-174,56
9,78E-04	1,73	-169,99	1,27E-03	0,99	-135,00
1,05E-03	0,82	-165,96	1,10E-03	3,85	171,03
3,28E-04	1,71	173,29	1,51E-03	1,66	154,98
2,07E-03	0,42	-135,00	4,85E-04	3,04	170,54
8,59E-04	1,82	-170,54	3,66E-04	0,73	164,06
3,96E-03	1,81	173,66	1,25E-03	1,36	-162,90
3,02E-04	0,91	173,66	8,28E-04	1,79	-153,44
4,90E-04	1,30	-147,53	4,51E-04	4,61	167,47
2,81E-04	1,57	-153,44	2,39E-04	2,94	170,22

Table A1: This table presents flux density and location of all imaged components in Fig. 8. Their position is given by the radius, the distance between them and $(0, 0)$ on the map, and their position angle relative to $(0, 0)$.

Flux density (Jy)	Radius (mas)	P.A. (degrees)	Flux density (Jy)	Radius (mas)	P.A. (degrees)
5,23E-04	5,00	-177,71	2,38E-04	1,49	19,65
4,74E-04	1,88	-154,80	-9,78E-05	1,56	-39,81
8,09E-05	4,50	178,73	9,31E-05	3,54	-132,71
2,69E-04	3,21	174,64	7,15E-05	3,86	-68,75
9,33E-04	4,63	166,26	-1,72E-04	11,60	-179,01
7,44E-05	3,90	-178,53	-2,53E-05	20,34	176,62
3,20E-04	3,42	159,44	-1,24E-04	5,52	5,19
7,22E-04	3,80	-178,49	1,32E-04	25,29	7,04
2,88E-04	1,26	-161,57	9,09E-05	3,22	-119,75
2,31E-04	3,38	161,03	1,08E-04	5,16	144,46
1,68E-04	3,41	176,63	9,18E-05	5,56	-37,69
2,00E-04	0,73	-164,06	-8,96E-05	20,24	176,32
1,26E-04	2,20	-177,40	-2,40E-05	22,48	-35,95
1,25E-04	4,60	178,76	7,86E-05	11,26	160,28
6,95E-04	5,10	-177,75	5,82E-05	25,59	-160,36
1,11E-04	2,84	-169,88	9,83E-05	2,73	-171,57
5,29E-05	3,93	172,69	-1,20E-05	14,52	-160,69
5,26E-05	2,31	-175,03	9,96E-05	16,48	-43,28
-9,66E-04	1,40	4,09	2,33E-05	3,70	-178,45
2,35E-04	4,90	-178,83	1,32E-04	13,40	142,28
1,91E-04	3,41	174,96	1,09E-04	1,57	153,44
-5,85E-04	3,85	81,03	8,65E-05	13,53	-79,35
2,85E-04	4,71	167,74	-7,88E-05	25,22	168,33
-3,23E-04	0,58	-59,04	7,76E-05	21,05	10,40
-1,99E-04	1,58	-34,70	-1,08E-04	22,40	-36,10
2,97E-04	4,27	159,44	-1,07E-04	11,74	135,00
1,53E-04	3,51	176,73	4,27E-05	11,35	160,45
3,18E-04	4,70	-156,16	-6,45E-05	9,33	30,96
1,15E-04	5,21	176,70	8,54E-05	16,20	-90,00
-2,76E-04	12,88	-133,11	1,17E-04	4,13	-6,95
1,68E-04	11,23	160,76	7,46E-05	4,61	-102,53
-2,88E-04	16,69	171,38	9,45E-05	5,24	145,10
2,48E-04	21,16	10,62	6,33E-05	2,90	-1,97
-3,27E-04	7,85	46,55	-5,24E-05	21,17	-14,50
1,94E-04	23,81	11,88	9,44E-05	25,42	-177,52
-2,93E-04	15,32	170,23	7,33E-05	25,46	-160,50
-2,91E-04	2,97	32,62	2,18E-05	5,18	-79,99
5,71E-05	5,22	175,60	3,20E-05	14,14	-36,95
-2,87E-04	0,64	51,34	-4,21E-05	1,49	-42,27
1,54E-04	3,31	174,81	3,21E-05	14,80	-63,09
-5,51E-05	10,08	-36,53	-5,22E-05	18,33	6,89
-2,32E-04	25,11	-18,58	6,21E-05	24,31	-170,77
-2,68E-04	6,24	-12,03	5,20E-05	6,08	170,54
-2,43E-04	10,00	-36,87	8,25E-05	18,65	-103,96
1,42E-04	4,05	-147,10	4,15E-05	24,53	-151,24

Table A2: Table A1 - continued.

Flux density (Jy)	Radius (mas)	P.A. (degrees)	Flux density (Jy)	Radius (mas)	P.A. (degrees)
6.17E-05	22.17	138.11	3.00E-05	15.88	98.69
-3.12E-05	11.12	-176.91	2.00E-05	23.38	7.13
4.12E-05	16.33	59.04	-3.00E-05	17.18	-151.50
-5.13E-05	12.12	171.94	-1.01E-05	7.64	52.98
-5.12E-05	25.32	168.38	1.99E-05	24.20	0.24
-4.10E-05	24.02	-28.06	-1.01E-05	24.22	170.73
3.05E-05	23.91	11.83	1.00E-05	5.64	-37.07
-4.04E-05	26.33	157.92	-1.00E-05	2.28	61.19
3.03E-05	5.20	-78.91	-1.98E-05	16.55	154.98
3.03E-05	14.67	-63.26	-9.93E-06	20.08	-11.20
-5.02E-05	18.65	-153.57	-9.85E-06	16.19	-25.62
-2.01E-05	24.04	170.42	9.82E-06	15.42	-99.71
3.02E-05	20.40	162.90	-9.82E-06	19.92	166.94

Table A3: Table A1 - continued.

Flux density (Jy)	Radius (mas)	P.A. (degrees)	Flux density (Jy)	Radius (mas)	P.A. (degrees)
1.967	0.00	0.00	-1.897E-03	1.94	-34.51
8.886E-02	0.10	-90.00	2.538E-03	3.91	175.60
1.392E-01	0.28	135.00	-4.261E-03	3.01	176.19
2.874E-01	0.20	-90.00	1.890E-03	9.03	175.55
1.041E-01	0.42	135.00	-1.391E-03	6.85	-173.29
1.581E-02	0.22	116.57	1.732E-03	0.91	-6.34
2.321E-01	0.36	123.69	3.331E-03	5.60	177.96
4.517E-02	0.22	-116.57	9.730E-04	2.10	154.65
1.375E-01	0.30	-90.00	-3.733E-03	4.80	177.61
6.020E-02	0.22	26.57	-4.748E-03	1.00	-53.13
4.657E-02	0.32	-71.57	1.628E-03	9.21	-2.49
1.342E-01	0.57	135.00	-1.960E-03	1.41	-171.87
1.660E-01	0.64	141.34	-1.102E-04	1.20	41.63
7.842E-02	0.28	-135.00	-9.793E-04	2.62	6.58
4.665E-02	0.32	-108.44	-2.132E-04	1.13	45.00
1.014E-01	0.85	-45.00	-1.995E-03	1.20	138.37
3.510E-02	0.36	-146.31	-2.322E-03	1.20	48.37
3.800E-02	0.32	18.43	2.367E-03	0.70	0.00
1.235E-02	0.41	14.04	1.178E-03	2.01	153.44
8.299E-03	0.78	-50.19	1.885E-03	0.78	140.19
8.457E-02	0.72	146.31	-2.046E-03	5.82	4.93
4.406E-02	0.36	-123.69	2.820E-03	2.14	-169.22
1.181E-02	0.42	-135.00	1.359E-03	8.93	175.50
7.036E-03	0.45	-153.44	1.348E-03	4.49	-168.44
8.852E-03	0.51	11.31	1.228E-03	10.13	4.53
5.629E-03	0.54	-158.20	5.475E-04	7.62	-3.76
8.392E-03	1.10	174.81	-4.842E-04	1.06	-48.81
1.643E-02	0.50	-143.13	-9.530E-04	4.42	-174.81
2.687E-03	1.00	-180.00	-1.252E-03	0.92	-49.40
1.469E-02	0.81	150.26	-6.306E-04	9.82	176.50
-5.000E-03	1.80	-3.18	-4.648E-04	7.96	7.21
3.972E-03	4.01	175.71	6.208E-04	1.81	6.34
2.492E-03	3.91	177.06	2.337E-04	19.02	177.29
-7.460E-03	0.50	53.13	-3.805E-04	2.08	-144.78
5.128E-03	2.70	-2.12	4.582E-04	5.12	12.41
3.420E-03	0.81	97.13	-3.779E-04	8.96	-6.41
-2.825E-03	6.75	-173.19	2.258E-04	8.94	174.86
4.512E-03	4.92	4.67	-1.488E-04	1.55	165.07

Table A4: This table presents flux density and location of all imaged components in Fig. 10. Their position is given by the radius, the distance between them and $(0, 0)$ on the map, and their position angle relative to $(0, 0)$.

Flux density (Jy)	Radius (mas)	P.A. (degrees)	Flux density (Jy)	Radius (mas)	P.A. (degrees)
8.239E-01	0.00	0.00	3.933E-04	1.53	148.39
6.651E-03	0.22	153.44	1.960E-04	0.95	161.57
1.075E-01	0.22	-26.57	6.478E-04	2.44	160.82
9.591E-02	0.45	153.44	3.321E-04	1.14	164.75
4.857E-02	0.50	143.13	1.194E-03	3.45	150.46
3.531E-02	0.22	-63.43	4.998E-04	8.39	149.15
4.583E-03	1.79	153.44	4.611E-04	1.44	146.31
4.032E-03	0.42	135.00	9.114E-04	1.24	165.96
2.283E-03	2.86	155.23	7.579E-04	8.47	149.50
1.327E-03	1.92	152.10	1.611E-03	2.53	161.57
2.461E-03	0.67	153.44	2.761E-04	3.67	154.13
4.920E-03	0.58	149.04	2.288E-03	7.46	144.82
3.036E-03	0.64	141.34	8.897E-04	1.33	167.01
2.210E-03	2.10	154.65	1.402E-03	7.32	147.83
4.489E-04	2.33	154.54	6.972E-04	1.36	143.97
2.156E-03	2.55	154.44	2.347E-04	3.76	154.80
1.353E-03	2.95	156.04	6.800E-04	7.19	148.08
3.612E-04	3.18	155.85	4.431E-04	2.42	150.26
9.910E-04	3.27	156.57	1.367E-03	1.30	147.53
1.629E-03	2.46	153.44	1.172E-04	3.81	175.49
1.145E-03	3.53	154.89	1.146E-04	3.28	148.74
7.320E-04	2.01	153.44	2.105E-04	3.91	175.60
6.237E-04	3.05	156.80	1.075E-04	3.19	147.80
1.587E-03	7.68	145.07	6.526E-04	3.85	155.43
3.788E-03	0.57	135.00	7.294E-04	4.01	177.14
2.131E-03	3.58	153.44	2.879E-04	3.11	146.82
2.516E-04	1.70	151.93	9.533E-05	2.62	162.26
8.901E-04	8.48	142.18	9.170E-05	3.20	159.86
1.331E-03	3.14	157.52	3.717E-04	8.56	149.84
1.079E-03	8.40	141.77	6.293E-04	7.38	139.40
4.321E-04	1.61	150.26	1.701E-04	3.98	162.47
1.006E-03	3.23	158.20	3.194E-04	3.02	145.78
2.690E-03	1.91	-173.99	1.433E-04	8.32	144.78
2.398E-03	0.72	146.31	2.058E-04	5.10	-178.88
2.501E-04	2.19	155.77	2.028E-04	7.10	147.65
4.714E-04	2.28	156.80	1.679E-04	3.01	158.55
2.136E-04	0.76	156.80	8.056E-05	3.82	173.99
2.091E-04	2.25	159.15	6.266E-04	3.94	156.04
1.595E-03	7.55	145.26	7.570E-05	2.51	151.39

Table A5: This table presents flux density and location of all imaged components in Fig. 12. Their position is given by the radius, the distance between them and $(0, 0)$ on the map, and their position angle relative to $(0, 0)$.

Flux density (Jy)	Radius (mas)	P.A. (degrees)	Flux density (Jy)	Radius (mas)	P.A. (degrees)
2.804E-04	3.83	172.50	2.514E-04	14.95	10.41
1.405E-04	4.08	162.90	-1.930E-04	20.06	138.84
5.753E-04	2.94	144.69	-1.351E-04	20.37	51.78
5.981E-04	5.00	-180.00	-9.485E-05	21.45	50.30
1.871E-04	3.10	159.23	1.995E-04	24.60	-146.44
6.211E-04	7.38	144.37	1.214E-04	7.38	49.40
4.712E-04	6.27	146.06	-7.150E-05	16.91	-83.55
3.749E-04	4.18	163.30	-1.496E-04	5.82	15.95
1.605E-04	0.50	126.87	5.710E-05	26.94	145.13
5.840E-05	3.91	177.06	-2.094E-04	12.40	73.61
1.929E-04	4.00	178.57	8.247E-05	25.65	-157.54
1.358E-04	4.03	156.62	-2.086E-04	23.66	-80.02
1.342E-04	0.99	-135.00	1.948E-04	21.69	84.71
4.514E-05	6.22	143.50	1.687E-04	17.53	-153.58
4.481E-05	5.20	-178.90	1.553E-04	14.20	-89.19
4.367E-05	2.86	143.53	-5.286E-05	24.19	34.22
-2.772E-04	1.50	3.81	1.786E-04	21.16	-27.90
8.063E-04	23.41	170.66	1.296E-04	19.68	77.38
-4.864E-04	1.40	4.09	-1.546E-04	11.26	142.21
-3.273E-04	1.66	-32.74	2.296E-04	20.51	-136.19
4.286E-04	26.91	-160.69	9.068E-05	23.70	102.92
4.628E-04	21.36	-60.55	-1.157E-04	17.35	-164.28
4.415E-04	14.07	45.29	1.151E-04	26.85	145.01
4.839E-04	19.90	152.79	8.886E-05	0.32	108.44
-4.646E-04	0.45	-63.43	2.038E-04	13.26	32.37
4.712E-05	21.31	-60.79	-1.141E-04	16.90	-83.88
1.450E-04	18.67	147.25	1.391E-04	24.88	53.50
-3.466E-04	7.78	107.97	-7.564E-05	26.93	117.42
-1.663E-04	19.98	138.65	-1.381E-04	25.15	22.69
3.909E-04	20.76	118.17	-2.612E-05	26.47	-108.50
3.583E-04	16.12	11.45	-1.249E-04	18.19	137.45
-1.804E-04	1.58	-34.70	-5.010E-05	25.61	165.53
1.285E-04	24.68	-146.57	-6.496E-05	6.28	59.35
4.173E-04	19.46	12.46	3.811E-05	9.87	-96.98
2.813E-04	24.01	174.50	8.752E-05	19.16	-111.75
2.410E-04	18.75	147.41	-4.964E-05	24.33	44.33
-2.639E-04	5.32	5.39	1.603E-04	20.90	-180.00
2.407E-04	25.33	108.65	-1.238E-04	19.73	-154.47
-2.270E-04	25.39	-71.64	7.414E-05	24.44	105.91
2.482E-04	1.22	145.01	1.108E-04	19.31	-105.62

Table A6: Table A5 - continued.

Flux density (Jy)	Radius (mas)	P.A. (degrees)	Flux density (Jy)	Radius (mas)	P.A. (degrees)
-7.376E-05	20.43	141.56	3.604E-05	15.94	-150.70
6.098E-05	13.40	-179.57	-2.420E-05	5.92	15.68
6.096E-05	27.84	143.91	2.392E-05	14.85	134.45
2.458E-05	25.74	-157.62	2.392E-05	6.71	-65.34
-1.217E-04	6.19	58.88	-2.382E-05	5.42	5.29
-7.259E-05	20.62	-24.95	1.197E-05	19.14	77.63
6.050E-05	16.41	27.19	-3.549E-05	12.59	38.87
-4.841E-05	21.89	100.80	2.364E-05	27.42	-48.70
-4.813E-05	15.72	-113.63	-2.364E-05	24.29	-28.25
-2.418E-05	26.50	-108.71	2.360E-05	24.96	-106.77
3.624E-05	12.08	83.35	-1.184E-05	9.70	1.77
-6.008E-05	12.16	45.67	1.173E-05	0.92	-130.60

Table A7: Table A5 - continued.

Flux density (Jy)	Radius (mas)	P.A. (degrees)	Flux density (Jy)	Radius (mas)	P.A. (degrees)
1.922	0.10	0.00	4.209E-03	1.12	79.70
3.473E-01	0.14	-45.00	2.659E-03	1.71	96.71
7.909E-02	0.36	123.69	3.073E-03	1.25	118.61
2.656E-02	0.70	90.00	2.120E-03	0.41	-14.04
4.915E-03	0.80	90.00	6.979E-04	1.73	100.01
2.142E-02	0.81	97.13	5.808E-04	3.28	58.74
2.615E-02	0.30	90.00	1.555E-03	5.88	125.31
2.526E-02	0.41	75.96	6.114E-04	5.72	109.39
1.622E-02	0.22	-26.57	1.562E-03	3.61	109.44
6.627E-03	0.91	96.34	1.017E-03	0.61	80.54
7.877E-03	1.00	95.71	1.203E-03	4.96	117.60
2.597E-03	0.71	98.13	5.771E-04	6.06	103.35
5.404E-03	1.10	95.19	1.746E-03	2.37	117.65
1.669E-03	0.89	116.57	6.130E-04	3.98	101.59
7.794E-03	0.32	-18.43	1.066E-03	6.09	104.27
5.572E-03	0.94	122.01	1.167E-03	5.69	108.44
7.278E-03	0.89	63.43	3.525E-04	3.96	100.18
4.701E-04	1.12	100.31	5.248E-04	3.33	57.26
8.731E-04	1.14	105.26	4.240E-04	3.50	88.36
2.899E-03	1.10	90.00	5.100E-04	6.38	99.02
4.722E-03	1.00	126.87	4.088E-04	6.15	111.98
7.293E-04	1.17	109.98	5.499E-04	3.96	132.96
2.175E-03	1.10	84.81	3.020E-04	4.92	116.57
1.255E-03	1.21	114.44	1.010E-04	3.20	110.14

Table A8: This table presents flux density and location of all imaged components in Fig. 14. Their position is given by the radius, the distance between them and $(0, 0)$ on the map, and their position angle relative to $(0, 0)$.

Flux density (Jy)	Radius (mas)	P.A. (degrees)	Flux density (Jy)	Radius (mas)	P.A. (degrees)
3.128E-04	2.62	96.58	1.969E-04	3.11	123.18
9.675E-04	0.45	63.43	-2.235E-04	25.34	-143.99
4.976E-04	7.74	-14.22	-1.816E-04	10.24	35.86
-1.617E-03	0.78	-50.19	-2.728E-04	14.11	-177.56
-8.486E-04	14.86	156.19	2.173E-04	18.70	-25.33
8.935E-04	7.64	-14.40	-1.932E-04	11.70	18.43
1.032E-03	7.31	93.14	1.961E-04	12.59	141.13
1.750E-04	20.05	-176.00	1.208E-04	3.88	55.49
5.200E-04	22.14	31.90	1.898E-04	21.59	140.26
8.752E-04	20.06	-175.71	1.201E-04	25.67	26.37
6.094E-04	4.41	166.91	2.347E-04	20.55	4.18
-1.631E-04	16.42	151.25	1.888E-04	21.84	24.34
8.685E-04	1.73	10.01	-1.409E-04	17.07	131.91
-3.197E-04	9.79	168.81	9.524E-05	6.02	105.42
-3.414E-04	16.06	117.84	-9.318E-05	8.70	-72.61
-4.544E-04	18.25	44.11	1.852E-04	3.58	-120.14
7.351E-04	0.36	56.31	1.153E-04	7.85	121.46
-1.257E-04	0.71	-45.00	6.889E-05	21.92	31.95
4.859E-04	11.50	115.23	-1.627E-04	17.25	-49.94
6.684E-04	26.64	-163.20	-1.377E-04	12.83	165.10
4.872E-04	10.06	116.57	-1.151E-04	21.81	-1.58
-2.341E-04	11.61	18.59	-1.376E-04	10.16	36.19
-2.226E-04	16.38	151.56	-6.860E-05	27.68	-33.06
-8.117E-04	0.72	146.31	1.352E-04	24.27	171.47
-5.563E-04	1.80	33.69	-4.555E-05	7.26	51.71
2.608E-04	4.22	31.43	9.089E-05	13.96	-65.45
-1.451E-04	15.06	175.05	1.129E-04	7.31	92.35
3.147E-04	2.10	-87.27	-6.818E-05	22.22	147.31
-4.208E-04	7.95	-68.60	6.783E-05	2.12	81.87
4.673E-04	6.62	128.25	-6.718E-05	18.10	-135.00
1.853E-04	26.48	27.92	6.642E-05	28.18	-25.20
-2.620E-04	15.01	-1.53	-4.449E-05	11.17	160.11
-3.129E-04	6.51	-45.00	6.674E-05	12.67	141.41
4.370E-04	25.22	170.87	-6.653E-05	5.91	56.04
3.861E-04	23.26	-27.67	6.600E-05	4.17	-44.03
1.902E-04	6.36	98.13	-2.215E-05	14.13	-86.35
5.302E-04	6.12	-51.63	-2.206E-05	9.97	-68.84
2.313E-04	3.35	-63.43	2.207E-05	4.89	40.86
2.814E-04	21.26	22.10	2.203E-05	16.72	22.88
-3.090E-04	9.48	-45.86	-2.192E-05	13.78	-28.61
2.508E-04	4.91	93.50	2.179E-05	12.88	-126.16
4.494E-04	1.14	74.74	-2.169E-05	9.92	176.53
8.175E-05	3.80	54.64	-2.168E-05	10.01	-68.30
-1.759E-04	10.84	14.42	-2.159E-05	20.63	-8.64
-3.943E-04	2.67	-167.01			

Table A9: Table A8 - continued.